



## Research paper

# On the influence of flow-front orientation on stringer stiffened composite panels in water impacts

Connor Pearson<sup>a,b,\*</sup>, Marius de Mourgues<sup>a,c</sup>, Mark Battley<sup>a,d</sup>, Veronique Michaud<sup>c</sup>, John Little<sup>e</sup>, Guillaume Verdier<sup>f</sup>, Tom Allen<sup>a,b</sup>

<sup>a</sup> Centre for Advanced Materials Manufacturing and Design, The University of Auckland, Auckland, New Zealand

<sup>b</sup> Department of Mechanical and Mechatronics Engineering, The University of Auckland, Auckland, New Zealand

<sup>c</sup> Laboratory for Processing of Advanced Composites, Ecole Polytechnique Federale de Lausanne, Lausanne, Switzerland

<sup>d</sup> Department of Engineering Science, The University of Auckland, Auckland, New Zealand

<sup>e</sup> PURE Design and Engineering, Wynyard Quarter, Auckland, New Zealand

<sup>f</sup> Guillaume Verdier Architecture Navale, Larmor-Baden, Morbihan, France

## ARTICLE INFO

## Keywords:

Slamming

Water impacts

Hat stringer

Stringer stiffened composite panels

Marine hull structures

## ABSTRACT

Water impacts form the critical load case for high-performance carbon fibre reinforced polymer (CFRP) racing craft. Such events produce a peaked, non-uniform pressure distribution that travels along a hull panel as it is immersed. Current design standards are based on static, uniform pressure loads that do not account for the directional nature of water impacts. With recent trends towards the use of directionally stiffened hull structures in the form of stringer stiffened composite panels (SSCPs), such simplifications of the load case may no longer be valid. In this study, a marine-based SSCP was tested experimentally and numerically to investigate the effects of flow-front orientation on high-performance hull panels. Parallel and perpendicular impacts at constant velocity were carried out using the novel Servo-hydraulic Slam Testing System (SSTS) and the results were used to validate a one-way coupled computational fluid dynamics — finite element analysis (CFD-FEA) Fluent/Abaqus solution. The highest strains in the monolithic skin and stringer were observed for perpendicular impacts. A parameter sweep across a range of impact orientations between parallel and perpendicular impacts was carried out. An approximately linear relationship between flow orientation angle and key structural strains was observed, with the highest strains reported at 70–90°. Results indicate that the critical load case for SSCP occurs at 75° orientation angles, where strains in the stringer capping are maximum.

## 1. Introduction

Water impacts, also known as slamming, form the critical design case for hull panels in small high-performance racing craft. They result in a peaked, non-uniform pressure distribution that travels along the hull panel as it is immersed, leading to significant out-of-plane loads. These loads are critical for racing craft as they are often constructed out of shear critical materials (Stenius et al., 2011), such as carbon or glass fibre reinforced polymer (CFRP or GFRP) composites.

The characteristics of a slamming event depend on several factors, such as free-surface conditions, craft velocities/accelerations, hull geometry, deformations, and vessel heading (Abrate, 2011), which introduce many non-linearities into the problem. The peak impact pressure and distributions are primarily dependent on the relative angle between the water surface and hull, known as the deadrise angle,  $\beta$ , and the impact velocity,  $V$  (von Karman, 1929). An outline of a two-dimensional rigid impact event for a V-wedge hull section is

detailed in Fig. 1. The bottom edge of the wedge forms the keel, while the top edge forms the chine (where the V-wedge meets the vertical side). The impact event is divided into two stages; the chines-dry and chines-wet (Stenius et al., 2011). In the chines-dry stage (Fig. 1), peak pressures occur at the contact point between the water surface and structure, also known as the water flow-front. During the impact, this flow-front and pressure pulse travel from the keel to chine. In the chines-wet stage, the flow detaches from the chine and impact pressures are relatively uniform. For water impacts where the deadrise angle is greater than 3°, air entrapment is not significant (Chuang, 1966a,b; Duan et al., 2020) and so peak impact pressures increase with decreasing deadrise angle and increasing impact velocity (von Karman, 1929; Wagner, 1931). Peak pressures and impact forces occur during the chines-dry stage. Additional factors such as water compressibility, jet formation, air cushioning, air bubbles and hydroelasticity may also

\* Correspondence to: 2nd Floor, Building 903, 314 Khyber Pass Rd, Newmarket, Auckland 1023, New Zealand.  
E-mail address: [connor.pearson@auckland.ac.nz](mailto:connor.pearson@auckland.ac.nz) (C. Pearson).

<https://doi.org/10.1016/j.oceaneng.2024.117797>

Received 31 January 2024; Received in revised form 22 March 2024; Accepted 3 April 2024

Available online 8 April 2024

0029-8018/© 2024 The Author(s). Published by Elsevier Ltd. This is an open access article under the CC BY license (<http://creativecommons.org/licenses/by/4.0/>).

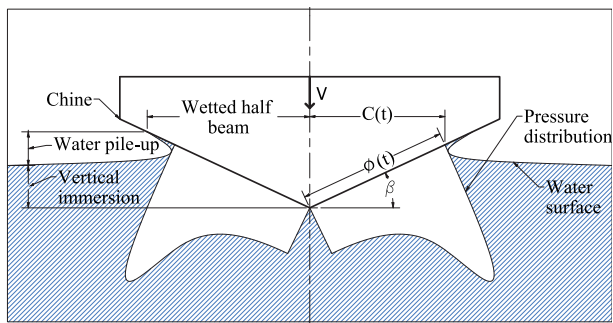


Fig. 1. Schematic of main parameters in the 2D wedge impact during the chines-dry stage.  $\theta(t)$  is the actual wetted length of the panel, while  $c(t)$  is the horizontal projection of wetted length.

be present and have some effect on the impact event (Faltinsen et al., 2004). This means that slamming is a complex, non-linear and stochastic event, making it difficult to study and design for. Current design and analysis methods of hull panels are conducted using an equivalent static uniform pressure (Allen et al., 1978; DNV-GL, 2015; ISO, 2019). Such methods are simplistic and based on traditional metallic planing craft, so their application to modern CFRP high-performance craft may not be appropriate. A shear critical CFRP hull structure might withstand an idealised distributed global load, but may not withstand the real localised pressure pulse. A more detailed application of the slamming load case in the design process is required to fully optimise the structural efficiency of hull panels.

Slamming can be studied using simple gravity drop tests or under constant velocity impacts. However, gravity drop tests are not representative of operational water impacts (Tveitnes et al., 2008; Battley and Allen, 2012). Marine craft are large, high speed structures with a significant quantity of inertia. While an entire craft will undergo deceleration upon impact, from the perspective of a single hull panel, the impact is experienced with an approximately constant velocity. Therefore, constant velocity impact studies of hull panels more accurately represent real world events. The behaviour of high-performance hull panels in constant velocity water impacts has been studied previously (Battley et al., 2005, 2009; Charca et al., 2009; Charca and Shafiq, 2010, 2011; Stenius et al., 2011; Battley and Allen, 2012; Stenius et al., 2013; Allen and Battley, 2015; Hassoon et al., 2017b,a, 2018, 2019), but these focused exclusively on sandwich structures. These structures are often quasi-isotropic (or close to it), and so are unaffected by flow-front direction. A square quasi-isotropic sandwich panel will behave the same way if the flow-front travels at  $0^\circ$  or  $90^\circ$  along the surface. Recent design trends have seen a shift away from sandwich structures to stringer stiffened composite panels (SSCPs). SSCP offer some advantages, including increased specific strength and reduction of core shear failures observed in sandwich constructions (Charca et al., 2009; Charca and Shafiq, 2010, 2011). However, SSCP are directionally stiffened structures. It is not known how the relative angle between the travelling flow-front and the stringer axis may impact the structural response of the panel. SSCP have been the focus of many studies (Zimmermann et al., 2006; Bertolini et al., 2008; Reinoso et al., 2012; Blázquez et al., 2012; Vescovini et al., 2013; Jin et al., 2015; Zhu et al., 2015; Mo et al., 2016; Ahmadi and Rahimi, 2019; Li et al., 2022), but these have primarily analysed in-plane loaded structures destined for the aerospace or automotive industries. The behaviour of SSCP in water impacts has yet to be studied.

The SSCP designs in this study were based off those found in recent IMOCA60 generations, one of the pre-eminent ocean-going racing yacht classes (International monohull open class association (IMOCA), 2021). These structures are comprised of several stringers bonded to the 'internal' side of a monolithic skin. The stringers feature a global cover laminate of carbon twill, with unidirectional capping reinforcement

along the crown (or cap). The cover plies primarily carry transverse shear loads through the web, while the capping carries longitudinal bending loads. The cross-sectional profile is formed by laminating over a machined foam former which remains within the structure after construction. The 'external' side of the skin forms the outer surface of the hull, and is in direct contact with water.

In this work, SSCP specimens were experimentally tested in constant velocity water impacts in parallel and perpendicular configurations as shown in Fig. 2. A SSCP digital twin was created in Abaqus CAE 2021 and loaded with a non-uniform slamming pressure distribution as it travels along the panel surface. This non-uniform pressure distribution was determined using an Ansys Fluent 2022 fluid model and mapped to the FEA model. A parameter sweep was conducted to explore the relationship between flow-front direction and stringer orientation across a range of angles. This was used to determine the most extreme load case orientation for SSCP.

## 2. Experimental set-up

### 2.1. Testing system

All experimental tests are carried out using the Servo-hydraulic Slam Testing System (SSTS) (Fig. 3a) located at the Centre of Advanced Materials Manufacturing and Design (CAMMD) within the University of Auckland. A servo-hydraulic ram is mounted vertically above a 3.5 m diameter, 1.55 m deep pool of water within a polyethylene tank, as shown in Fig. 3a, giving a fluid domain of approximately 14,900 L. The ram is used to drive a carriage sitting in guiding linear bearings into water up to a maximum velocity of 10 m/s. Specimens are mounted to the underside of a fixture at a  $10^\circ$  deadrise angle, as shown in Fig. 3b. A flow restriction panel was installed at the rear of the specimen to simulate a wedge impact. The SSTS was specially built to investigate water impacts in a highly controlled and repeatable manner, and has been used in many studies (Battley et al., 2005, 2009; Stenius et al., 2011; Battley and Allen, 2012; Stenius et al., 2013; Allen and Battley, 2015; Swidan et al., 2016, 2017). More details of the operational parameters of the SSTS have been published by Battley and Allen (2012).

### 2.2. SSCP specimen manufacture

The SSCP design used in this study is illustrated in Fig. 4a. Tests were carried out with stringers oriented parallel and perpendicular to the flow with a constant  $660 \times 660$  mm panel size. The geometry and laminate were scaled down from the in-service design to fit the specimen within the SSTS, as shown in Fig. 4b. The central  $535 \times 535$  mm test section of the specimen SSCP is a square panel with four reinforcing stringers. 25 mm thick GFRP/foam sandwich bulkheads are included on all four sides of the central test section, forming a hollow box. The specimen is bolted to the SSTS fixture through the top surface of the bulkheads. Limitations of the SSTS configuration mean that a 660 mm panel span is too narrow to include flow restriction panels at the ends of the specimen. Conversely, a  $1050 \times 1050$  mm specimen (the distance between flow restriction panels) would result in too high loads for the testing system. This means 3D flow effects were present in the test.

The specimen was constructed using 150 gsm standard modulus (SM) carbon unidirectional prepreg (PCU150) and 200 gsm SM carbon twill prepreg (PCC200) manufactured by Hankuk Ltd. GFRP/foam sandwich bulkheads were cut, shaped and bonded to each edge of the panel using two layers of 200 gsm SM wet-laminated CFRP twill weave with a 40 mm lap. Three additional layers of 30 mm long PCC200 patches were added to the cover laminate in the vicinity of the bulkhead due to the high shear loads expected at these locations.

Standard out-of-autoclave marine manufacturing practices were followed during the construction of the SSCP specimen and are listed below.

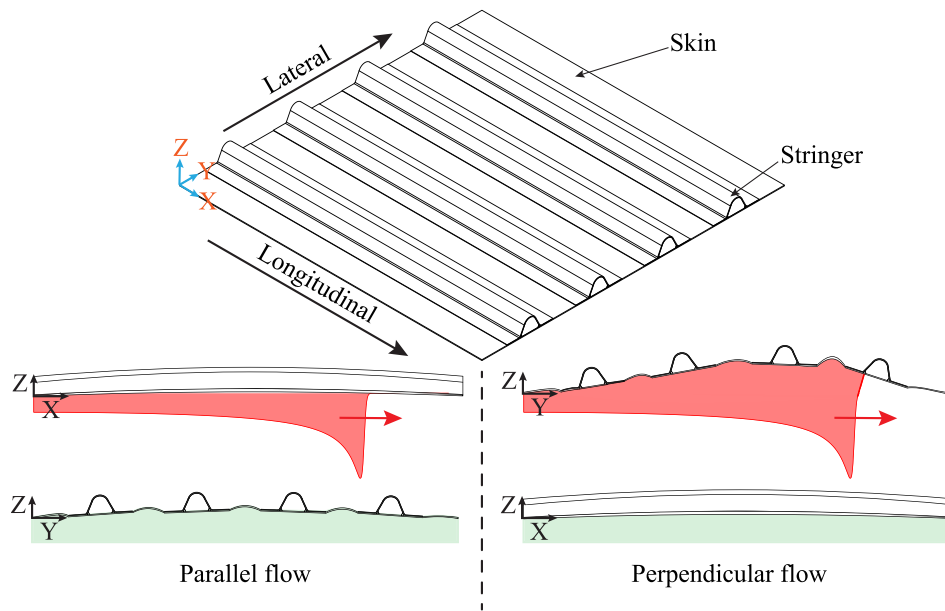


Fig. 2. Schematic of a square SSCP outlining the panels longitudinal and lateral axis, and possible deformations for parallel and perpendicular orientation impacts due to the propagating pressure pulse (shaded in red). Pressures orthogonal to the pulse travel direction are uniform along the panel span (shaded in green).

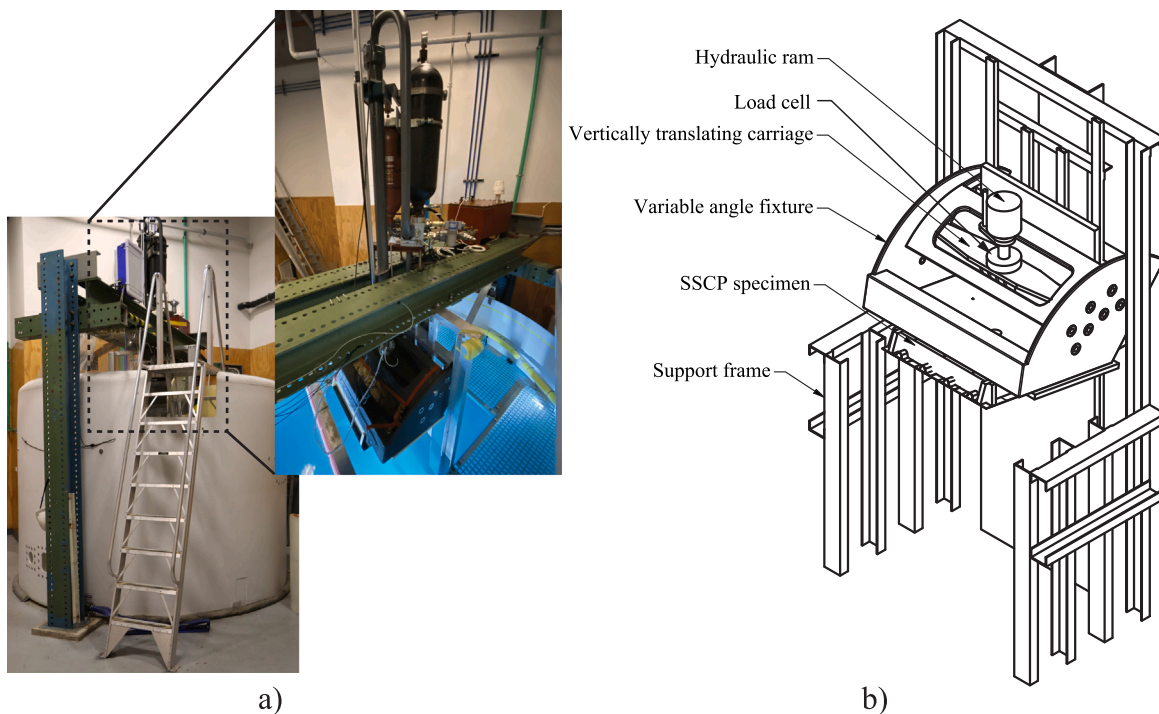


Fig. 3. (a) Exterior and interior views of the SSTS and actuator mechanism, and (b) schematics of SSTS.

- Manufacture of a  $750 \times 750$  mm PCC200 monolithic skin. CFRP prepreg was cured under vacuum at  $85^\circ\text{C}$  for 12 h.
- Machined M80 SAN foam formers were bonded to the monolithic skin with a spacing of 150 mm using 300 gsm SA80 glue film. The glue film was cured under vacuum at  $85^\circ\text{C}$  for 12 h.
- A 6 mm radius cove was formed using a high-performance rubberised epoxy HPR5 and colloidal silica mixture (1:1 volume ratio) between the base of the foam former and monolithic skin.
- The stringer was laminated with the capping layers evenly dispersed into the cover laminate. CFRP prepreg was cured under vacuum at  $85^\circ\text{C}$  for 12 h. The panel was then trimmed to its final  $660 \times 660$  mm size.
- GFRP sandwich panels were cut and shaped to produce an inverse of the stringer profile. The shaped bulkheads were clamped and bonded perpendicular to the stringers using HPR5/silica and shaped to produce a 6 mm radius cove. Longitudinal framing made from the same material was interlocked with the transverse bulkheads and bonded to the CFRP skin parallel to the stringers.
- The bulkhead and framing joints were reinforced using two layers of 200 gsm wet-laminated carbon twill tape with a 40 mm lap into the stringer.
- The top surface of the bulkhead and frames were machined flat and aluminium C-section brackets were bonded in place using

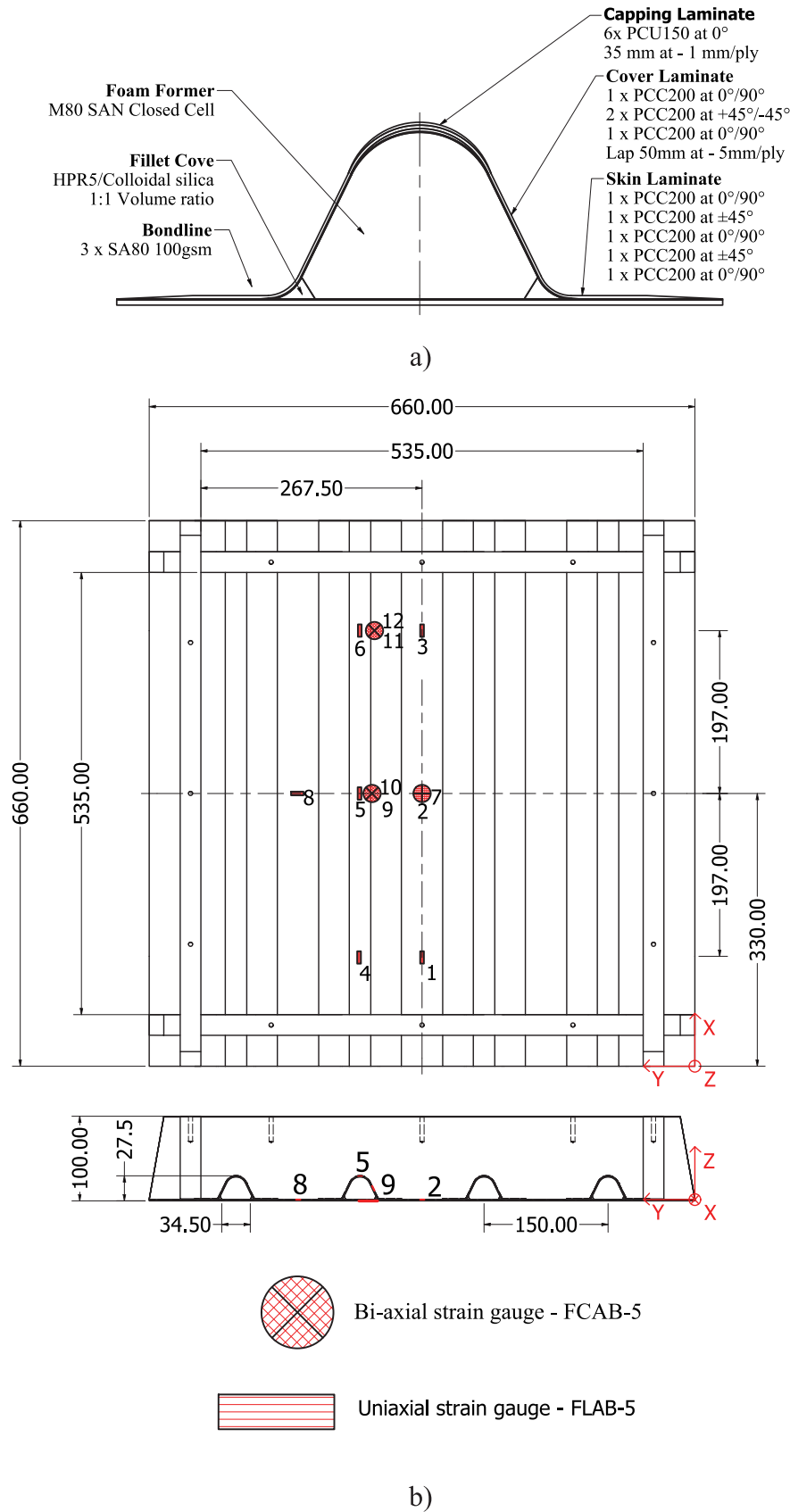


Fig. 4. Specimen (a) cross-sectional laminate details and (b) SSCP overall dimensions and strain gauge placement.

HPR5/silica. These were drilled and tapped to bolt the specimen to the base of the SSTS variable angle fixture.

### 2.3. Instrumentation

Position, load and strain was acquired with a National Instruments (NI) cDAQ-9178. This was integrated within a LabView control interface and synchronised with the SSTS test trigger.

SSTS stroke length and specimen position was measured by a Balluff BTL1PCW 500 Hz micropulse transducer through a NI 9235 cDAQ module. Specimen velocity was calculated for every test to confirm the SSTS control system was operating as intended.

Impact forces are measured by a 25,000 kg 500 Hz PT Global Ltd load cell directly connected to the piston through a pinned eye bolt. The SSTS carriage and mounted specimen are fixed to the bottom of the load cell. Due to the load cell's location in the test, only the vertical component of the impact force is measured, and also includes inertial loads from the specimen and carriage, subsequent impact loads from fixture (as it enters the water) and frictional loads from the linear bearings.

Tokyo Measuring Instruments FLAB-5-11 uniaxial and FCAB-5-11 biaxial 120Ω resistive strain gauges were bonded to the 'internal side' of the panel specimen at several locations along the stringer and skin to capture data of the strain field during the water impact event. These were bonded across the stringer crown, web and monolithic skin, as shown in Fig. 4b. The strain gauge signals are conditioned by three NI 9237 cDAQ modules for a total of 12 strain measurements sampling at 25 kHz.

- Monolithic skin longitudinal strains ( $\epsilon_{XX}$ ) measured by strain gauges 1, 2 and 3 (MLong1, MLong2 and MLong3).
- Stringer longitudinal strains ( $\epsilon_{XX}$ ) measured by strain gauges 4, 5 and 6 (SLong4, SLong5 and SLong6).
- Monolithic skin lateral strains ( $\epsilon_{YY}$ ) measured by strain gauges 7 and 8 (MLat7 and MLat8).
- Stringer web shear strains ( $\epsilon_{XZ}$ ) measured by strain gauges 9, 10, 11 and 12 (SWeb9, SWeb10, SWeb10 and SWeb12).

### 2.4. Testing procedure

The SSCP specimen was tested in parallel and perpendicular flow configurations at 1 m/s, 2 m/s and 3 m/s at a 10° deadrise angle, for a total of 6 tests. Each test was performed 5 times to assess the repeatability of the set-up and the collected data. Higher impact velocities were not attempted to reduce the likelihood of specimen failure. Measurements of impact forces and strain responses indicated a high degree of repeatability between tests, as shown in Fig. 5. The dashed line indicates when the panel has become fully immersed in water based on the undisturbed free surface and marks a definite end to the chines-dry stage.

The water free-surface was located 500 mm below the SSTS origin. At the start of each test, the specimen is accelerated to the required constant speed, and from 500–610 mm stroke length, the specimen is in the chines-dry stage of the impact event. From 610–800 mm, the specimen enters the chines-wet stage and the SSTS fixture begins to impact the water, and from 800–1000 mm the ram is decelerated to a stationary position. As this study is interested in the effects of the pressure pulse on the SSCP, only the chines-dry stage of the impact was considered. Fig. 6 displays the flow at touchdown, the chines-dry stage and chines-wet stage. Spray along the sides of the specimen can be seen in Fig. 6b, highlighting the presence of 3D flows in the test.

## 3. Numerical methodology

The numerical methodology features a one-way coupled CFD-FEA approach, where pressure distributions from a constant velocity rigid panel in the chines-dry stage of an impact event were mapped to a structural model of the SSCP test specimen. Fig. 7 outlines the coupling approach used in this project.

### 3.1. CFD methodology

There are several existing methods for modelling water impact events. Previous studies have obtained accurate results using computational fluid dynamics (CFD) (Nair and Bhattacharyya, 2018b,a; Pearson et al., 2022; Wen et al., 2022; Hosseinzadeh et al., 2023a,b; Chen et al., 2023; Wen et al., 2023), smoothed particle hydrodynamics (SPH) (Weber, 2017; Hassoon et al., 2019) and coupled Eulerian Lagrangian (CEL) methods (Stenius et al., 2007; Allen and Battley, 2015; Weber, 2017; Li, 2018; Hosseinzadeh et al., 2023b). Despite their ability to model the fluid and structural responses simultaneously, SPH and CEL methods have been shown to be highly sensitive to set-up parameters and produce significant noise in the outputs (Allen, 2013; Weber, 2017). CFD solvers are proven as robust and accurate for modelling water impacts (Pearson et al., 2022; Wen et al., 2022, 2023). The 3D non-uniform pressure distribution for this work was determined numerically using Ansys Fluent 2022 CFD with the volume of fluid (VOF) technique. The flow was treated as inviscid with no surface tension effects as slamming is an inertia-dominated problem (von Karman, 1929; Wagner, 1931) and the omission of viscous effects has a negligible impact on final results (Hosseinzadeh et al., 2023b). The unsteady incompressible Euler equations solved by Fluent are presented in Eq. (1).

$$\frac{\delta}{\delta t}(\rho \vec{V}) + \nabla(\rho \vec{V} \vec{V}) = -\nabla P + \rho \vec{g} \quad (1)$$

where  $\rho$  is density,  $\vec{V}$  is the fluid velocity vector,  $P$  is the fluid pressure,  $\vec{g}$  is the gravity acceleration vector (0, -9.81, 0).

The VOF method was developed by Hirt and Nichols (1981) and is one of the most widely used free surface tracking methods (Fondelli et al., 2015) as it can handle significant free surface distortions and collapse. The free surface interface is tracked using an explicit formulation for the volume fraction scalar value  $\mu$  using Eq. (2). For two-phase flow, cells where  $\mu = 0$  are filled with air, while cells where  $\mu = 1$  are filled with water. Cells where  $0 < \mu < 1$  contain a free surface.

$$\frac{1}{\rho_q} \left[ \frac{\delta}{\delta t}(\mu_q \rho_q) + \nabla(\mu_q \rho_q \vec{V}_q) = S_{\mu_q} + \sum_{p=1}^n (\dot{m}_{pq} - \dot{m}_{qp}) \right] \quad (2)$$

where  $\dot{m}_{qp}$  and  $\dot{m}_{pq}$  is the mass transfer from phase  $q$  to  $p$  and from phase  $p$  to  $q$  respectively.

A global moving mesh method (GMM) was implemented to handle the motion between the impacting body and free-surface. This methodology was first implemented by Qu et al. (2015) to study the motions of aircraft ditching in water, and has successfully been used to model a variety of water impact events (Qu et al., 2015; Nair and Bhattacharyya, 2018b; Wen et al., 2022, 2023). In the GMM methodology, the fluid domain (the mesh cells and boundaries) move vertically downward as a rigid body while the free-surface remains stationary in the global frame of reference. This avoids costly remeshing approaches for single mesh domains and boundary updates for overset chimera meshes (Pearson et al., 2022). Motion equations for the global mesh are provided in Eq. (3).

$$V_y = -2 \text{ [m/s]}, V_x = V_z = 0 \text{ [m/s]}, V_{xy} = V_{xz} = V_{yz} = 0 \text{ [rad/s]} \quad (3)$$

Details of the domain, boundary conditions and mesh are presented in Fig. 8 and Table 1. Surface adef were defined as a wall to replicate the rear-most flow restriction panel used in the experiments. Surfaces cdeh, bchg and efhg are defined as pressure inlets with VOF and pressure boundary conditions to ensure the water level and hydrostatic pressures remains constant in the global frame of reference as the mesh travels downwards during the impact. Domain dimensions are a function of panel length,  $L$ , where  $L = 660$  mm. Due to symmetry along the panel centreline and flow restriction panel along keel, a quarter model featuring a  $660 \times 330$  mm panel surface was simulated to reduce computational costs. Pressure distributions for a 2 m/s, 10° impact were extracted at 0.5 ms time increments. The solver was run

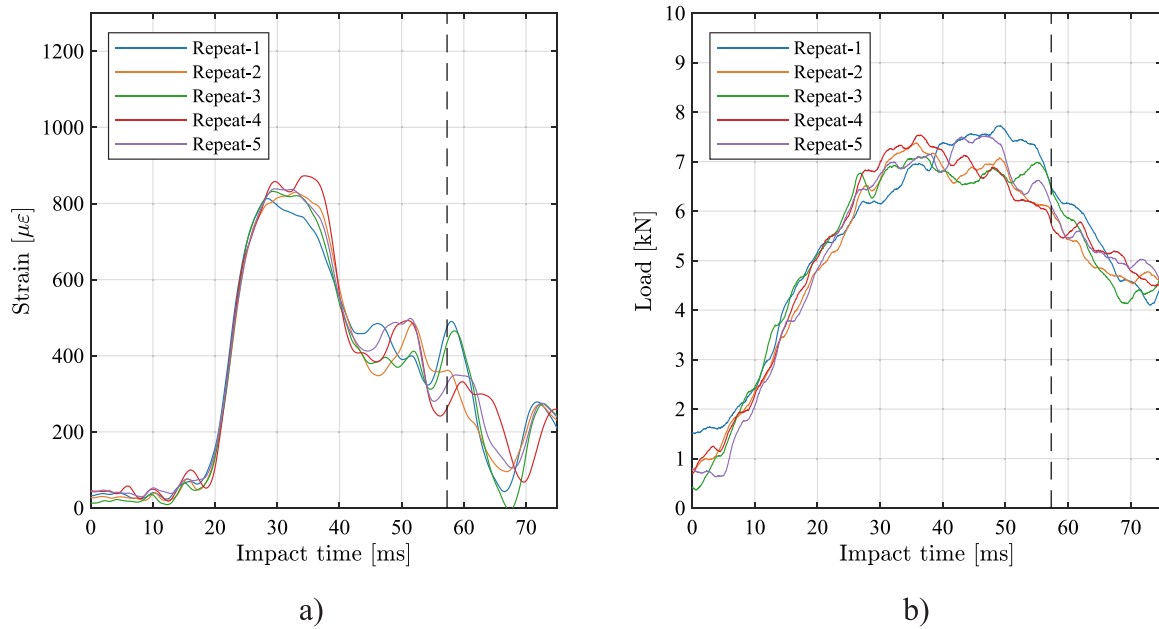


Fig. 5. (a) Strains across repeats at SLong5 at 2 m/s, 10° (b) Impact forces across repeats at 2 m/s.

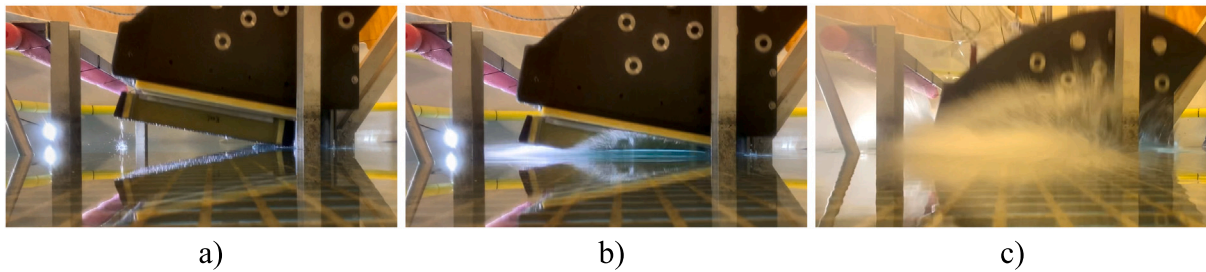


Fig. 6. Specimen water impact as seen from side-on at three positions (a) Initial touchdown, (b) Chines-dry stage and (c) Chines-wet stage.

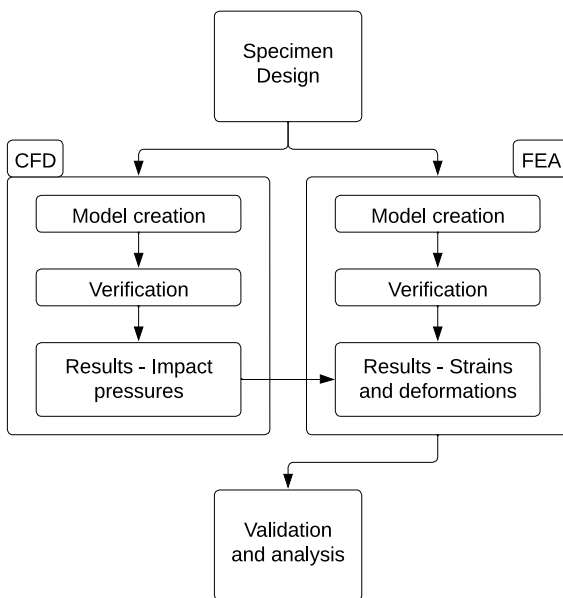


Fig. 7. One-way coupling procedure.

Table 1  
CFD boundary conditions (refer to Fig. 8).

Surface	Boundary condition
abcd	Symmetry
adef	Wall
abgf	Pressure inlet
efgh	Pressure inlet
bchg	Pressure inlet
cdeh	Pressure inlet
Panel	Wall

keel. A SIMPLEC pressure–velocity coupling method was selected, and the VOF was discretised using the *Compressive* technique. The unsteady terms are discretised using a first-order implicit scheme, the convection terms are discretised using a third-order Monotonic Upstream-centered Scheme for Conservation Laws (MUSCL) scheme, and the pressure term is discretised using a body force weighted scheme

Mesh convergence and validation of the numerical approach was conducted using a 2D wedge impact at 2 m/s with a deadrise of 10° (surface abcd). Three grids with increasing cell size at the panel surface (1, 2.5 and 5 mm) were simulated and impact forces and pressures were extracted. Details of this mesh convergence are presented in Table 2. As seen in Fig. 9, the impact force solution converged for the cell size of 1–2.5 mm, with the maximum slamming coefficient matching that seen by Wen et al. (2022). Results for peak pressures improved as the cell size was decreased but final convergence was not achieved. However, the results did appear to be converging, with

for the entire chines-dry stage of the impact (50 ms) using a step size of 0.02 ms. The initial free surface level was located 1 mm below the

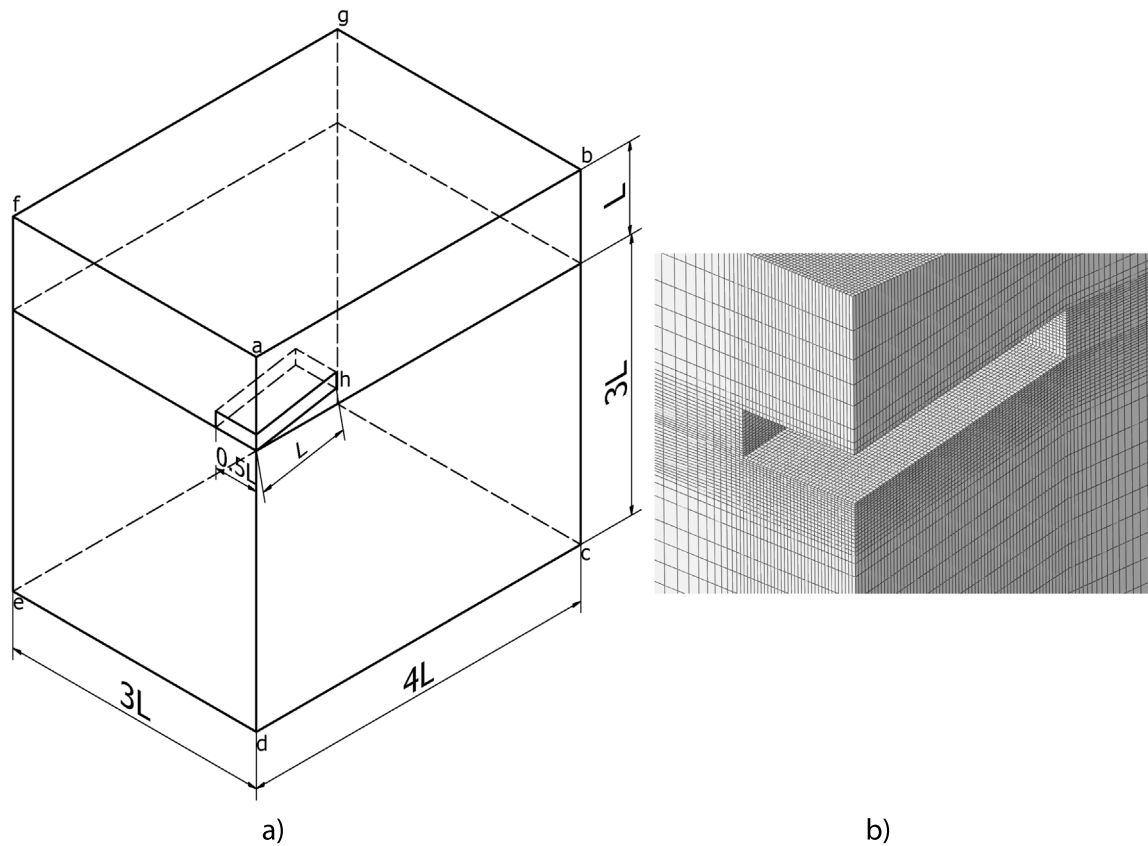


Fig. 8. (a) Domain dimensions as a function of panel length ( $L = 660$  mm) and (b) Close-up view of cells adjacent to the panel surface.

Table 2  
CFD mesh convergence results.

Panel cell size (mm)	Max slamming coefficient	Max pressure coefficient	N° of cells along panel
1	22.88	76.64	660
2.5	23.34	68.14	264
5	22.69	53.76	132

a 22.4% difference between the 2.5 mm and 5 mm mesh, and 11.1% percent difference between the 1 mm and 2.5 mm mesh. Further mesh refinement was deemed as too computationally expensive. It is worth stating that this peak pressure is concentrated and often occurs within a single cell, leading to numerical interpolation errors (Pearson et al., 2022). Additionally, accurate resolution of the non-uniform pressure distribution has been found to have a negligible effect on the structural response (Li, 2018; Chen et al., 2023). Residual pressures converge for a 2.5 mm cell size at  $C_p = 16.15$ . To balance computation cost and efficiency, a 2.5 mm cell size on the panel surface was selected for the final analysis with a domain of 6,836,496 cells with 6,998,226 nodes.

A comparison of pressure contours at 10, 20, and 30 ms through the chines-dry impact event are shown in Fig. 10. Effects of the 3D flow can clearly be seen in Fig. 10, as there are pressure drops along the panel edges compared to the centre. The pressure pulse develops a rounded front edge as flow along the sides travels slower than the centre due to outwash. Peak pressures increase during the impact, from 51.8 kPa at 10 ms, 54.6 kPa at 20 ms and 58.8 kPa at 30 ms. Maximum pressures along the edges are 30% of peak pressures at 15 kPa. Centreline residual pressures at the keel decrease during the impact from 22.1 kPa at 10 ms, 13.8 kPa at 20 ms and 10.4 kPa at 30 ms.

### 3.2. FEA methodology

The structural finite element model was implemented in Abaqus CAE 2021. Four independent parts are joined with mesh ties: stringer,

panel, bondline and bulkheads to produce a SSCP with 4 stiffeners, as seen in Fig. 11. Each part was modelled as an individual entity and connected using mesh tie constraints to allow sudden changes in mesh densities at interfaces, such as between the bondline and the panel/stringer laminates. CFRP and GFRP components were modelled using S4R conventional shell elements. The bond between the stringer and panel is modelled using second-order C3D6 3D 6-node linear triangular prism elements and 0.3 mm thick COH3D8 8-node 3D continuum cohesive elements. The foam former has not been included in the model, as this part is not structural and has a negligible effect on the structural response. The top surface of the bulkheads are fixed in place to replicate the attachment to the SSTS variable angle fixture. A similar FEA methodology has been adopted by other SSCP studies (Blázquez et al., 2012; Vescovini et al., 2013; Li et al., 2022). Material properties used within the FEA are presented in Table 3. The PCU150 and PCC200 properties were determined by ASTM standard tests (ASTM-3039, ASTM-D6641, ASTM-2344 and ASTM-D7078) while material properties for the bonding resin, foam and GFRP were provided by their respective manufacturers. Pressure distributions were imported from the CFD solution using nodal co-ordinate data at 0.5 ms time increments. The data were mirrored across CFD symmetry plane and the co-ordinate systems rotated so the flow travelled either parallel or perpendicular to the stringer axis in FEA. The final transformed co-ordinate data was applied to the lower surface of the panel in FEA as a mapped analytical field. Pressure distributions are reconstructed and

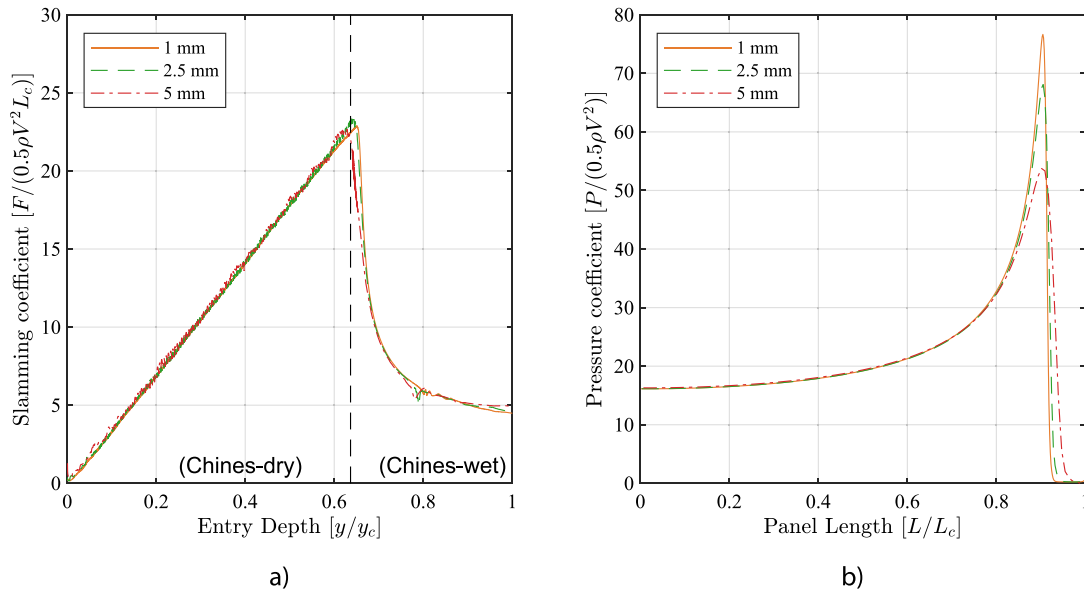


Fig. 9. (a) Slamming force coefficients for a 2 m/s, 10° 2D wedge during the initial impact, (b) Pressure coefficients for a 2 m/s, 10° 2D wedge just prior to the chines-wet stage.

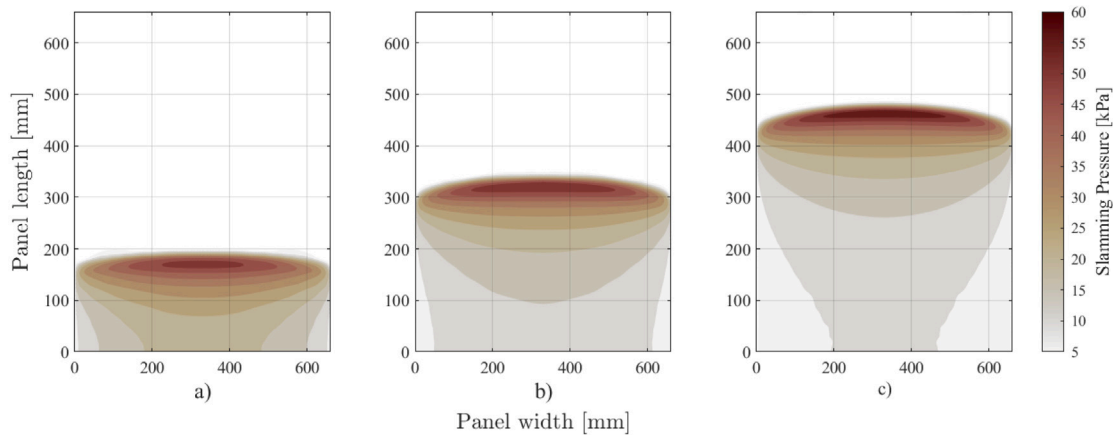


Fig. 10. Pressure distribution for a 3D water impact at (a) 10.0 ms, (b) 20.0 ms and (c) 30.0 ms.

Table 3

FEA material properties.

Material	$E_{11}$ (MPa)	$E_{22}$ (MPa)	$\nu_{12}$	$G_{12}$ (MPa)
PCU150	12900	8700	0.30	4.41
PCC200	61000	61000	0.10	3.99
HPR5	2800	2800	0.30	1080
M80 foam	31	31	0.30	12
GFRP	35000	35000	0.10	4000

applied to the FEA model based on interpolation between data points. In total, 100 time steps have been used to model the first 50 ms of a water impact of the SSCP specimen.

Mesh convergence of the FEA model was determined using a uniform pressure load of 100 kPa on the panel. Four grids with increasing global cell size (1, 2, 3 and 4 mm) were modelled, and the longitudinal strains in the capping laminate were extracted. The 99th percentile value for maximum and minimum stringer and skin strains was also extracted and are presented in Table 4. As seen in Fig. 12, the difference in maximum longitudinal capping strain is less than 0.01% between a 3 mm and 2 mm cell size, and there is no change between 1 mm and 2 mm results in Fig. 12. Therefore, the model was considered to have converged using a 2 mm global cell size. The final model has 550,516

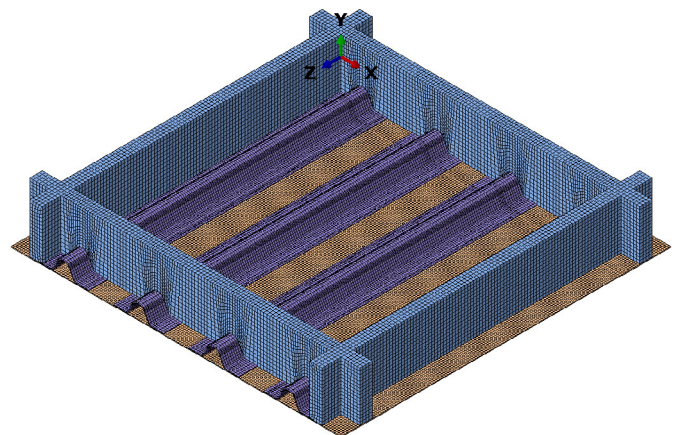


Fig. 11. FEA model geometry. For improved visibility, every second element is displayed.

elements and 642,180 nodes, with 268 elements along the length of the skin and stringers within the test section.

**Table 4**  
99.9th maximum and minimum strain percentiles used for mesh convergence.

	4 mm [ $\mu\epsilon$ ]	3 mm [ $\mu\epsilon$ ]	2 mm [ $\mu\epsilon$ ]	1 mm [ $\mu\epsilon$ ]
Min skin	-1870	-1830	-1880	-1880
Max skin	2670	2780	2780	2780
Min stringer	-2370	-2450	-2400	-2400
Max stringer	3600	3630	3630	3630

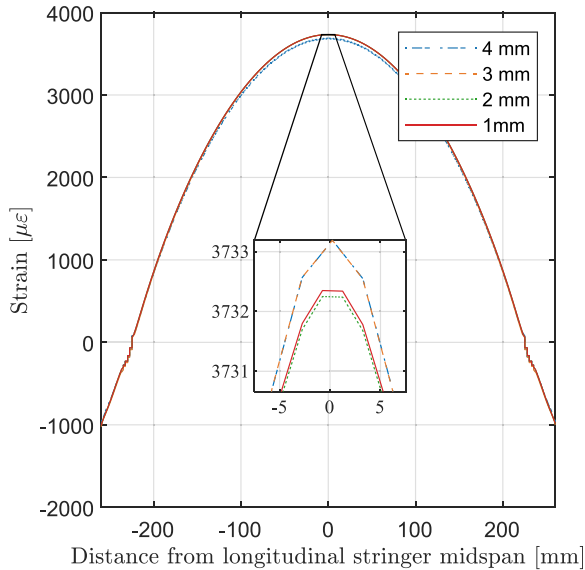


Fig. 12. FEA mesh convergence.

Time responses using quasi-static and transient solvers were compared and the results are presented in Fig. 13. The quasi-static solution was determined using a standard static non-linear implicit solver, while the transient solution was determined using a non-linear dynamic implicit. Both methods were solved for 100 steps with a 0.5 ms time increment. As seen in Fig. 13, the solutions are similar. Due to impact conditions, and panel mass and stiffness impact velocities studied in this work, the quasi-static solution appears valid, likely due to the low mass of the SSCP specimen and relatively slow impact velocity. The quasi-static method was adopted in this study to reduce the computational costs. All subsequent numerical results have been run using a standard static non-linear implicit solver.

### 3.3. Limitations of modelling method

The quasi-static, one-way coupling approach used here has been successfully used in previous work to study the structural response of the water impact (Stenius et al., 2013). However, it only remains valid so long as hydroelastic effects are small (Stenius et al., 2013). A limitation of the methodology used here is that the effects of hydroelasticity were unable to be modelled in full. The structural response was unable to interact with the fluid response and the applied pressure distribution as the coupling was one-way. Hydroelasticity can be divided into inertial and kinematic effects (Battley et al., 2009; Stenius et al., 2011). Inertial effects are related to the natural frequency of the structure and the frequency of loading (Berezniński, 2001; Stenius et al., 2011). Kinematic effects are related to changing boundary conditions at the fluid–structure interface, such as local geometry, velocity, and acceleration changes (Allen and Battley, 2015) which can cause changes in the response due to local changes in deadrise angles and the fluid response. Due to the relatively slow impact event studied here, small predicted panel deflections ( $\leq 3$  mm for the monolithic skin as predicted by FEA) and subsequent agreement between experimental

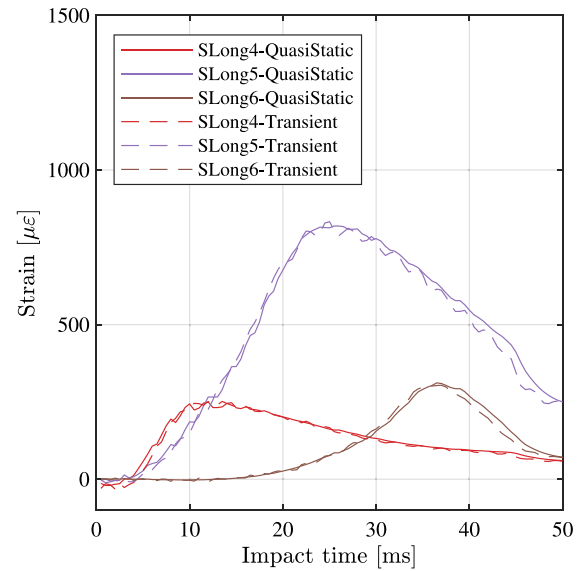


Fig. 13. Longitudinal stringer capping strains for Quasi-static and Transient FEA solvers.

and numerical results, the effects of hydroelasticity for this slamming event appear to be minor, and have a negligible effect on the final solution. A two-way CFD-FEA simulation was therefore not required to model the structural response to the impact event accurately.

## 4. Results and discussions

### 4.1. Impact forces

An approximate  $V^2$  relationship for impact force was observed between tests carried out at different velocities (Fig. 14a), which agrees with results seen throughout the literature (Abrate, 2011). Direct comparison of experimental and numerical impact forces in Fig. 14b is complicated by the configuration of the SSTS and the presence of parasitic forces (Allen and Battley, 2015). The load cell is located between the translating carriage and hydraulic ram (see Fig. 3), and so any measured force includes bearing friction and inertial forces. Furthermore, the rest of the testing fixture begins to contact the water free surface immediately after the SSCP specimen has become fully wetted ( $>45$  ms), and so impact force decay in the chine-wet stage is not expected to be similar. For this reason, the experimental measurements are expected to be a similar order of magnitude, but larger than simulated forces, as seen in Fig. 14b.

### 4.2. Overview of experimental and numerical strains

The discussion and comparison of results will focus on data for a 2 m/s impact of the panel shown in Fig. 4. Strain magnitudes at 1 m/s impacts are within the signal noise, while 3 m/s impacts featured more significant variation in impact velocity during water entry due to the increased load. Impacts at 2 m/s provide an appropriate balance between these issues. Details of strain gauge placement and flow orientation for parallel and perpendicular impacts is presented in Fig. 15. Longitudinal and lateral midspans ( $Long_0$  and  $Lat_0$ ) have been defined. Strain gauges have been divided into three categories (A, B and C) based on their position along the panel. Lines A, B and C on Figs. 16 and 20 indicate when the position of the pressure pulse has reached that respective group of strain gauges, as predicted by CFD.

A good agreement is seen between experimental observations and numerical predictions for strains at gauge locations, with the largest difference of 216 microstrain and 308 microstrain for parallel and

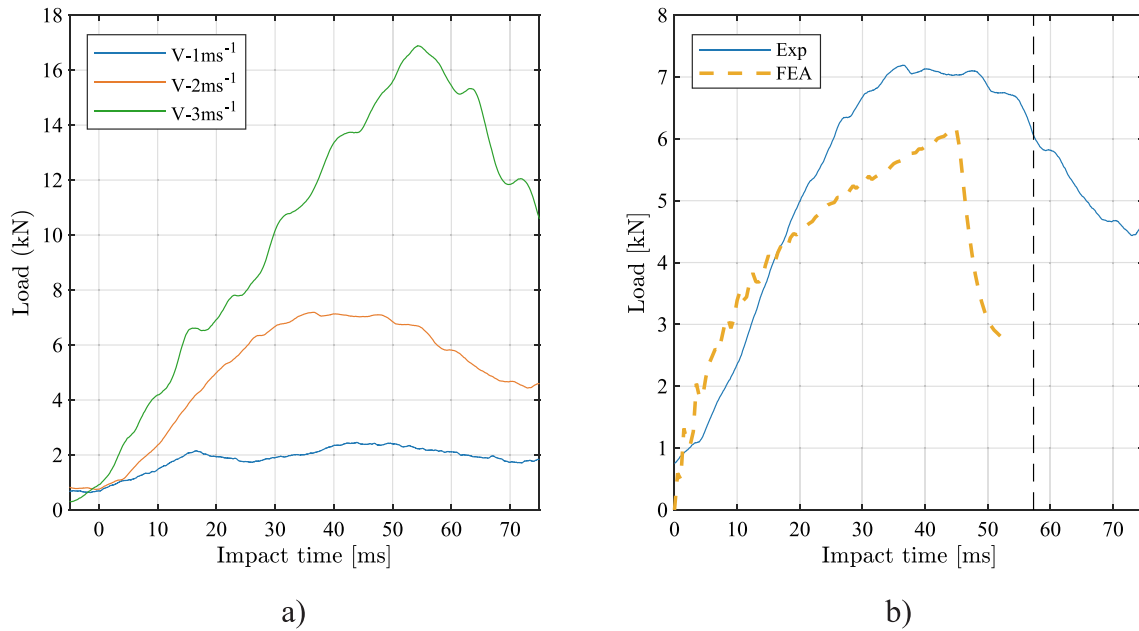


Fig. 14. (a) Impact forces across three different velocities and (b) comparison of experimental maximum impact forces to numerical results and analytical predictions.

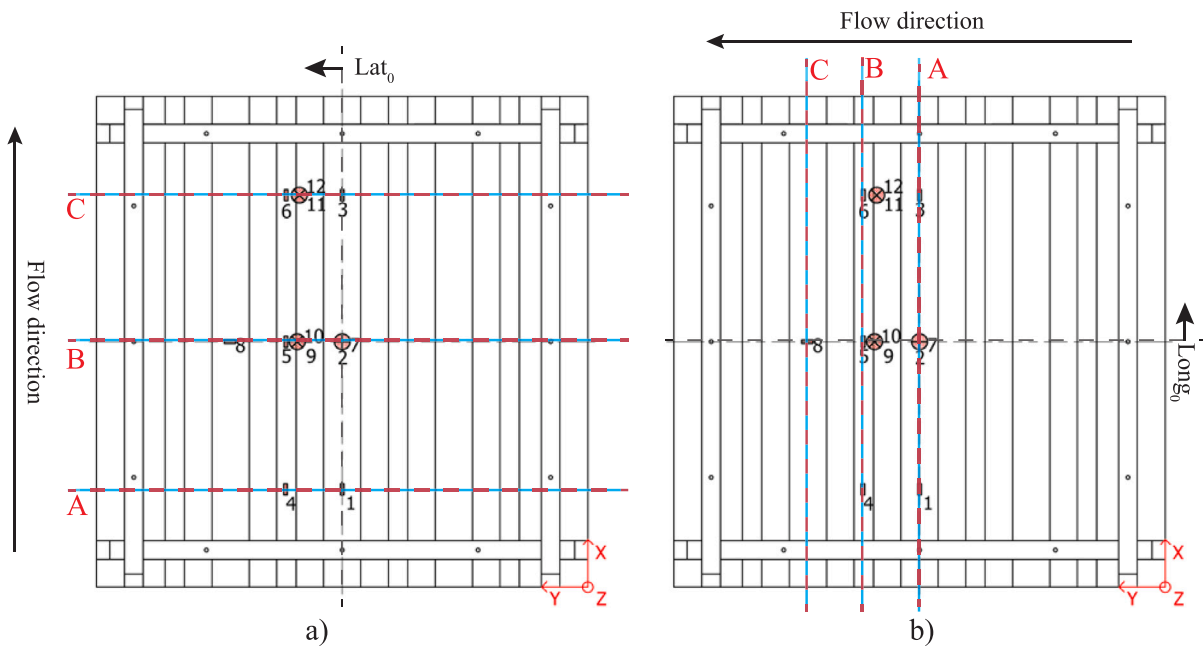


Fig. 15. Strain gauge setup and flow orientation for (a) parallel orientation tests and (b) perpendicular orientation tests.

perpendicular orientation impacts respectively at 2 m/s. 10° deadrise (Table 5). Strain behaviour throughout the impact event was well matched between experimental and numerical, with similar trends observed (Figs. 16 and 20). Zero time was defined as touchdown of the specimen, which is moment of initial contact with the free surface. This has been determined experimentally using the ram displacement, and numerically based on simulation start time.

#### 4.3. Parallel impact strains

In a parallel configuration impact, the pressure pulse travels along the longitudinal axis of stringers. The angle between the longitudinal axis and flow-front direction of travel is 0°. Strain responses for a single 2 m/s 10° deadrise parallel impact during the chines-dry stage is presented in Figs. 16a–d. Monolithic skin, capping and web shear strains

at 10, 20 and 30 ms as predicted by FEA are presented in Figs. 17–19. These results have been centred on the longitudinal and lateral midspans (Long<sub>0</sub> and Lat<sub>0</sub>) of the panel. The pressure distribution is overlaid onto these figures to indicate the load case at these times.

##### 4.3.1. Longitudinal monolithic skin strains in parallel impacts

Longitudinal strains in the unsupported monolithic skin (MLong1, MLong2 and MLong3 in Fig. 16a) feature a compressive dip, then a large tensile peak as the pressure pulse arrives at that location. This compressive dip in front of the pressure pulse occurs throughout the impact, as seen in Figs. 17a–c. As the SSCP impacts the water and force is applied, the structure is placed into global bending due to out-of-plane pressure loads. This introduces a tensile strain at the stringer crown and a compressive strain in the skin as the neutral axis of the

**Table 5**

Differences in maximum experimental and maximum strains for parallel and perpendicular orientations for a 2 m/s, 10° deadrise water impact.

Gauge	Parallel tests			Perpendicular tests		
	Experimental ( $\mu\epsilon$ )	FEA ( $\mu\epsilon$ )	Difference ( $\mu\epsilon$ )	Experimental ( $\mu\epsilon$ )	FEA ( $\mu\epsilon$ )	Difference ( $\mu\epsilon$ )
MLong1	464	403	-61	251	242	10
MLong2	359	148	-211	-282	-260	22
MLong3	564	348	-216	261	241	-20
SLong4	146	250	103	116	296	180
SLong5	692	819	127	813	1121	308
SLong6	329	312	-17	136	296	160
MLat7	1116	1028	-88	1360	1185	-175
MLat8	1063	937	-126	1395	1218	-178
SWeb9	121	109	-12	94	88	-6
SWeb10	153	212	58	61	88	27
SWeb11	-404	-499	95	-715	-764	-48
SWeb12	436	475	40	691	747	55

stringer lies in the web. However, at the location of the pressure pulse, there was a significant local load, inducing local bending. In these tests, the superposition of the local and global bending introduces an overall tensile strain in the top lamina of the skin at the location of the pressure pulse. The effects of this can be seen in Fig. 17, where compressive strains occur away from the pressure pulse, but tensile strains peak at the location of the pressure pulse. Additionally, the effects of the non-uniform pressure distribution produces asymmetric deflection in the skin. The largest deflections at any time are located at the pressure pulse and rapidly decay towards the unloaded section (Fig. 17). Interestingly, skin and stringer deflections are the same in the unloaded section. Note that the tensile peak of MLong2 was up to 63% less than MLong1 and MLong3 (Fig. 16a). This is because MLong2 experiences a higher global bending compressive load at the panel midspan, which decreases the overall tensile strain once the pressure pulse arrives. This can be seen by comparing Fig. 17a and b. These results indicate that the longitudinal response of the monolithic skin are dominated by the location of the pressure pulse in parallel orientation water impacts.

#### 4.3.2. Longitudinal stringer capping strains in parallel impacts

Longitudinal strains in the stringer capping (SLong4, SLong5 and SLong6 in Fig. 16b) are tensile throughout the impact event, with the largest experimental strains of 700  $\mu\epsilon$  seen by SLong5 at the centre of the span. As the impact event occurs, the longitudinal stringer strain behaviour is more gradual than the longitudinal skin strains, with a wider and less pronounced peak. By analysing strains and deflections in Fig. 17 it is clear the pressure pulse has some effect on the capping response, however this likely to be a function of total applied load rather than location of the pressure peak. Maximum strains and deflections along the cap are skewed by the pressure peak at 10, 20 and 30 ms (Fig. 17a–c), but unlike the skin response, there does not appear to be a significant local loading effect. Maximum capping strains and deflections in Fig. 17c occur 80–100 mm behind peak pressure. The stringers are significantly stiffer than the monolithic skin, and so the load from the pressure pulse is able to be distributed and carried along the entire length of the stringer. This implies that the stringer response is more affected by the total loading along the stringer than the location of the pressure pulse. SLong5 and SLong6 gradually increase throughout the impact, and do not rapidly decay after the pressure pulse has passed. Peak strain responses near the chine (SLong6) are 125% greater than those near the keel (SLong4) as the entire structure is more loaded at this point in the impact event (Fig. 17c). Note how peak strains near the supports (SLong4 and SLong6) are tensile. If the supports were completely fixed, then compressive strains would be expected due to reaction moments near this point. The tensile behaviour along the entire stringer length at 10, 20 and 30 ms (Fig. 17) and absence of any compressive strains implies there is some rotation of the supports into the panel span,

likely due to the lack of additional structures. Real-world hull structures are fully bounded by neighbouring panels and so are likely to have stiffer supports and boundary conditions. This would tend to reduce longitudinal capping strains at the midspan, and increase compressive strains at the supports. There is a greater disparity between SLong4-exp and SLong4-FEA compared to other capping locations, likely due to differences in flow formation and development just after touchdown or pressure losses may have occurred between the specimen keel and flow restriction panel that were not accounted for in the CFD.

#### 4.3.3. Lateral monolithic skin strains in parallel impacts

Compared to the longitudinal strains, the lateral strains in the unsupported monolithic skin region (MLat7 and MLat8 in Fig. 16c) do not appear to experience any significant loading prior to the arrival of the pressure pulse, with very little strain or deflection along the lateral midspan (Fig. 18a). This means lateral skin strains are not affected by the progressively increasing global load on the panel. Once the pressure pulse arrives (time B in Fig. 16c and Fig. 18b) the loading is relatively uniform and the small span between stringers compared to between bulkheads results in a high radius of curvature from the local pressure loading. This induces a larger tensile strain compared to the longitudinal response at the same location (1120  $\mu\epsilon$  strain for MLat7 vs. 359  $\mu\epsilon$  for MLong2). This peaked tensile response drops away to a lower values once the peak has passed (Fig. 18c). Both peaks occur simultaneously (time B) as MLat7 and MLat8 are located the same distance from the keel, and so the pulse arrives at both gauges at the same time. MLat7 is greater than MLat8 in all tests, As MLat8 is located closer to the edge of the panel and may experience more effect from 3D flows. This is seen in the pressure distribution in Fig. 18b, where pressures at MLat8 ( $Lat_0 = 197$  mm) are 89.4% of MLat7 ( $Lat_0 = 0$  mm), as the pressure distribution falls away close to the panel edges. Lateral deflections and strains are maximised at the middle of the unsupported region between stringers, and minimised under the stringers.

#### 4.3.4. Web shear strains in parallel impacts

Shear strains in the stringer web region (SWeb9, SWeb10, SWeb11 and SWeb12 in Fig. 16d) are expected to be maximum at the supports (chine and keel), and minimum in the centre of the panel as the shear forces are highest and lowest at these respective locations. As these gauges are measuring shear, SWeb9/10 and SWeb11/12 are expected to report equal but opposite strain magnitudes. The results from the gauges correlate well to expectations, with SWeb9 and SWeb10 reporting low strains as they are located at the centre of the panel. SWeb9 and SWeb10 report increasing equal and opposite strains until time B (Fig. 16), when the pressure pulse is directly underneath the midspan of the stringers (Fig. 15). The value for SWeb9 then inverts to return a slight positive strain, while SWeb10 decays away to a negligible value. SWeb11 and SWeb12 gradually increase throughout the impact as the stringer is progressively loaded, reporting the highest strains when the

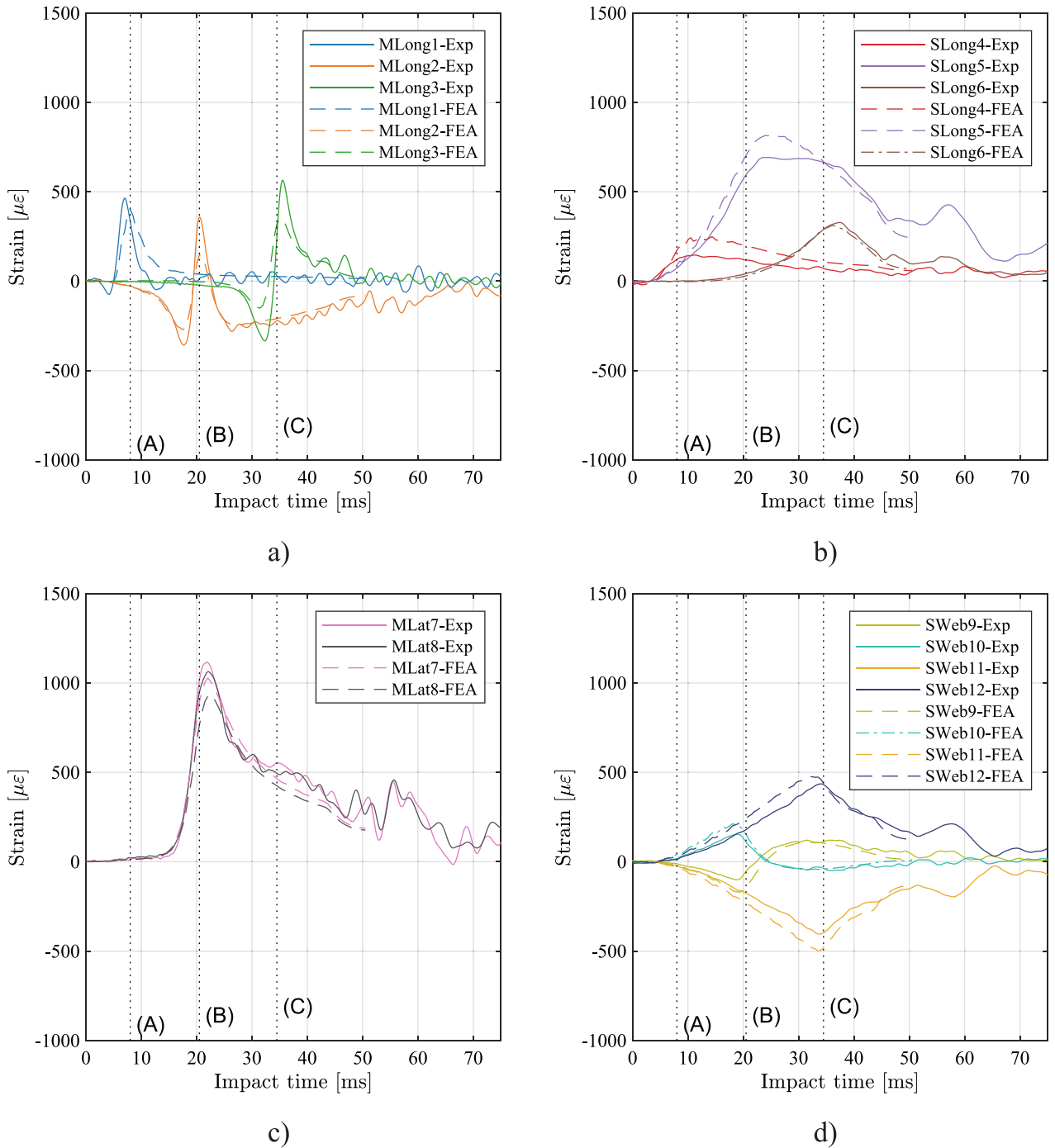


Fig. 16. Experimental and numerical strains from a Parallel flow impact at  $2 \text{ ms}^{-1}$  (a) Longitudinal monolithic skin strains (b) Longitudinal stringer capping strains, (c) Lateral monolithic skin strains and (d) Stringer web shear strains.

pressure pulse lies directly underneath at time C, just before the end of the chines-dry stage. This correlates well with expectations as this is the point of maximum impact force and shear load (Fig. 5d). Fig. 19 highlights shear strains along the stringer length at three times during the impact (10, 20 and 30 ms). Near the beginning of the impact, the pressure peak is located towards the keel ( $\text{Long}_0 = -200$ ), and so maximum strains of  $360 \mu\epsilon$  and  $200 \mu\epsilon$  are predicted there (Fig. 19a). As the impact continues and the pressure pulse moves along the stringer, shear strains at the chine ( $\text{Long}_0 = +200$ ) increase, while those at the keel remain relatively constant at  $360\text{--}400 \mu\epsilon$  respectively. Maximum impact shear strains occur towards the end of the impact (Fig. 19c) when the pressure pulse lies underneath the chine.

#### 4.4. Perpendicular impact strains

In perpendicular impacts, the flow-front direction of travel is at  $90^\circ$  relative to the longitudinal axis. As the pressure pulse travels along the panel, each stringer and unsupported skin section is simultaneously loaded along its entire length as shown in Fig. 15b. Strains for a single  $2 \text{ m/s}$ ,  $10^\circ$  deadrise perpendicular impact during the chines-dry impact stage tests are presented in Fig. 20a to d. Longitudinal, lateral and shear strains for the skin and stringer at 10, 20 and 30 ms as predicted by FEA are presented in Figs. 21–23. As in Figs. 17–19, these have been centred on the longitudinal and lateral midspans ( $\text{Long}_0$  and  $\text{Lat}_0$ ) of the panel

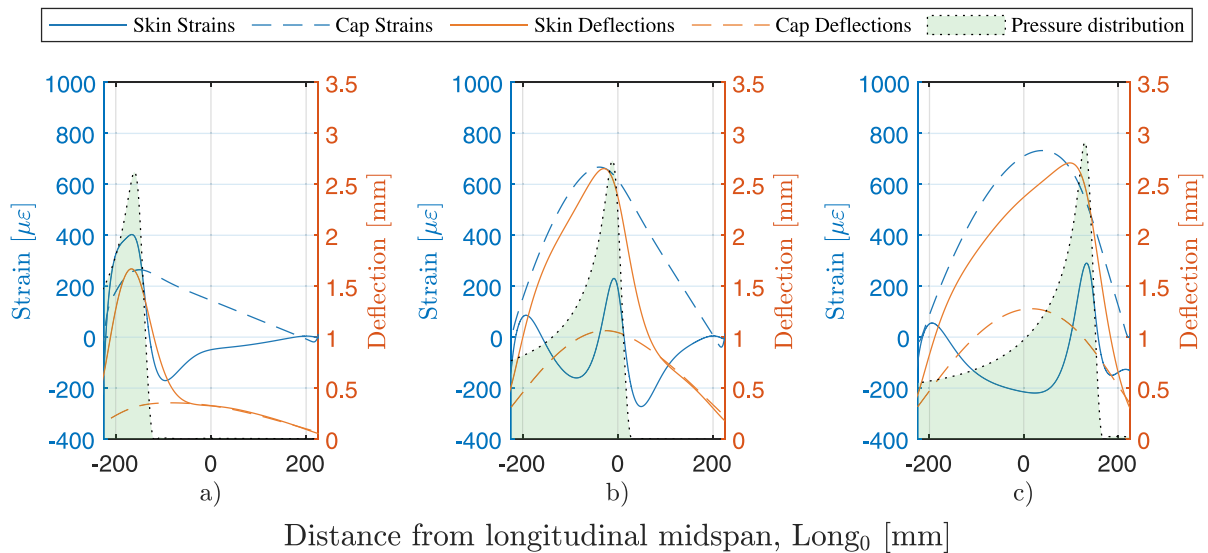


Fig. 17. Monolithic skin and stringer capping strains and deflections along the longitudinal axis for parallel orientation impacts with representative pressure distributions at (a) time = 10 ms, (b) time = 20 ms, (c) time = 30 ms.

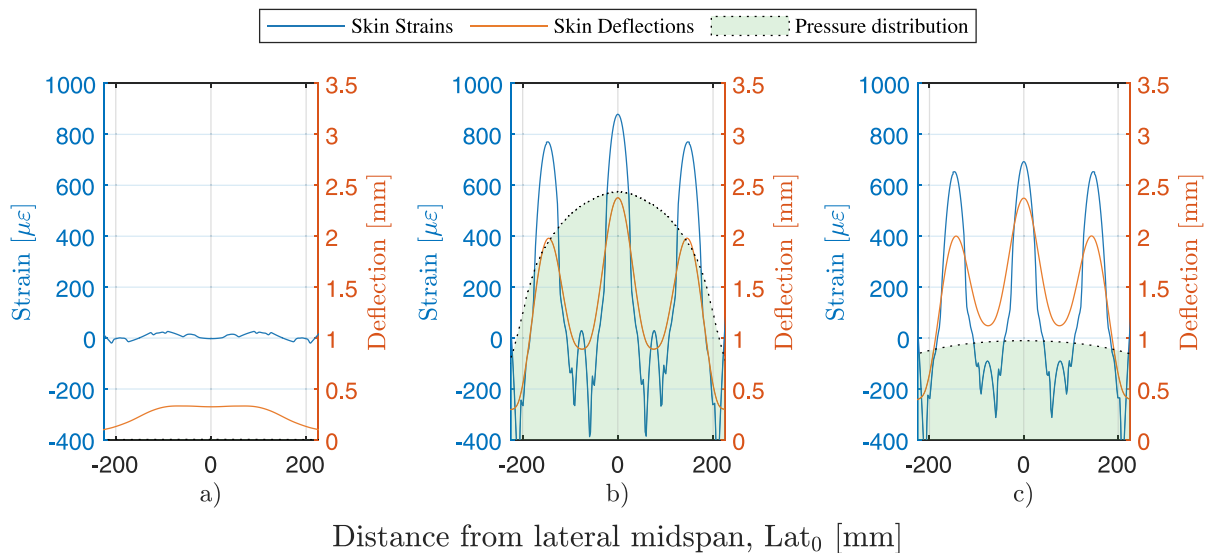


Fig. 18. Monolithic skin strains and deflections along the lateral axis for parallel orientation impacts with representative pressure distributions at (a) time = 10 ms, (b) time = 20 ms, (c) time = 30 ms.

and the pressure distribution is overlaid onto these figures to indicate the load case at these times.

4.4.1. Longitudinal monolithic skin strains in perpendicular impacts

In perpendicular orientation impacts, the longitudinal strains in the unsupported monolithic skin (MLong1, MLong2 and MLong3 in Fig. 20a) were aligned with the pulse and so experience a relatively uniform pressure along the longitudinal axis. Peak strains are reported just after the passing of the pressure pulse, as this is the point of maximum load carried by the monolithic skin. However, this behaviour was less peaked than the parallel flow orientation. No compressive dip was observed before the arrival of the pressure pulse, and midspan strains remain compressive throughout the impact. MLong1 and MLong3 report a small tensile peak of 200  $\mu\epsilon$  just after the passing of the pressure pulse. This behaviour is seen in Fig. 21b, where the skin strains are tensile near the bulkheads. This peak then drops away as the pulse passes and the lower residual pressures are applied (Figs. 21c). MLong2 remains compressively loaded throughout the impact with a small reduction in compressive strain when the pressure peak passes, from

-120  $\mu\epsilon$  in Fig. 21b to -220  $\mu\epsilon$  in Fig. 21c. This behaviour implies that longitudinal skin strains are less sensitive to the pressure pulse in perpendicular orientation impacts.

4.4.2. Longitudinal stringer capping strains in perpendicular impacts

Stringer longitudinal strains in the capping region (SLong4, SLong5 and SLong6 in Fig. 20b) are tensile throughout, with the largest strains seen at the centre of the span. In this orientation, the stringers are aligned with the pressure pulse and are loaded simultaneously by a relatively uniform pressure along their entire length as the pressure arrives (Fig. 21b). This means the presence of the pressure pulse has a increased local effect on the stringer strains compared to parallel orientations. There is a more peaked strain response when compared to parallel impacts (700  $\mu\epsilon$  vs. 1120  $\mu\epsilon$  from FEA). Strain responses gradually increase from time A, and report maximum strains at time C (Fig. 20). This indicates that loading of stringers only begins once the pulse crosses the midline of the neighbouring unsupported skin region, and peak loads occur just as the pulse passes the midline of the next adjacent skin region (Fig. 15). At this point, the highest slamming

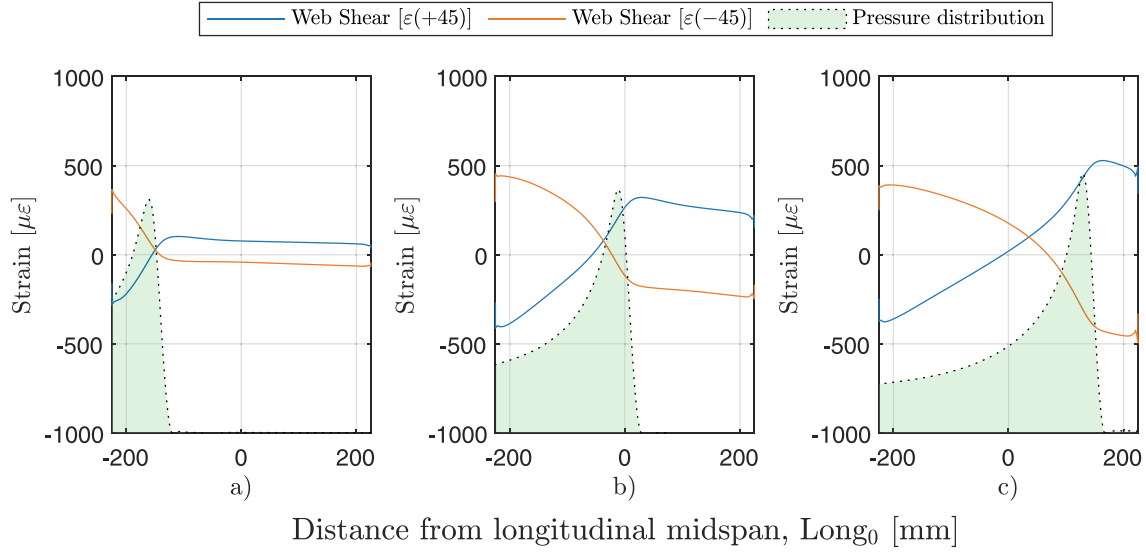


Fig. 19. Stringer web shear strains along the longitudinal axis for parallel orientation impacts with representative pressure distributions at (a) time = 10 ms, (b) time = 20 ms, (c) time = 30 ms.

pressures and loads are applied to a stringer, although this observation may depend on the relative size of the pulse and stringer spacing. Strain behaviour of SLong4 and SLong6 strains are approximately equal throughout the impact because of the symmetry in load along the stringer length. Comparing FEA predictions and experimental observations, the FEA overpredicts maximum stringer longitudinal capping strains by 27.5% higher for SLong5 and 58.7% higher for SLong4 and SLong6, with a more pronounced peak in the time responses.

#### 4.4.3. Lateral monolithic skin strains in perpendicular impacts

The lateral strains in the unsupported monolithic skin (MLat7 and MLat8 in Fig. 20b) report maximum strain magnitudes just after the pressure pulse has passed their respective locations (times A and C). These strain responses feature a pronounced tensile peak, and rapidly decay once the pressure pulse has passed over to a new unsupported panel region. MLat8 is slightly larger than MLat7 (1380 μϵ vs. 1330 μϵ from experiments), possibly reflecting the higher loads on the entire panel as it has become more immersed. Figs. 22a–c indicate that maximum strains and deflections occur at midspan of the skin nearest to the pulse. Maximum strains at 10, 20 and 30 ms are similar despite occurring at different locations along the lateral axis (125 μϵ, 120 μϵ and 150 μϵ respectively), indicating that the unsupported skins separating stringers behave relatively independently from each other. Skin deflections and strains decrease as the pressure pulse moves away, and the local pressure decreases (Fig. 22c).

#### 4.4.4. Web shear strains in perpendicular impacts

Once again, shear strains in the stringer web region (SWeb9, SWeb10, SWeb11 and SWeb12 in Fig. 20d) are expected to be maximum at the supports, and minimum in the centre of the panel. The results from the gauges correlates well to this expectation, as SWeb9 and SWeb10 report negligible strain close to zero throughout the test, while SWeb11 and SWeb12 gradually increase through the impact, reporting peak strains (±700 μϵ) when the pressure pulse lies directly underneath the stringer (time B). This peak has a higher magnitude and is more pronounced than the parallel orientation (700 μϵ vs. 430 μϵ), as the pressure pulse loads the entire stringer simultaneously, before passing on and leaving lower residual pressures at this location.

#### 4.5. Comparison of parallel and perpendicular orientation water impacts

In both orientations, lateral monolithic skin strains (MLat7 and MLat8) were the largest strains during an impact, with the largest

absolute strains occurring in perpendicular orientation impacts (1390 μϵ for perpendicular vs. 1100 μϵ for parallel from experiments). Midspan lateral monolithic skin strains (MLat7 and MLat8) and stringer web shear strains at the supports (SWeb11 and SWeb12) have larger and more pronounced strain responses in perpendicular impacts than those seen for parallel impacts (Table 6). The largest percent change in maximum strains for parallel vs. perpendicular orientations was observed for web shear (62.8%). Only longitudinal monolithic skin strains experienced higher strains in parallel orientations, but these magnitudes are not critical. The maximum strain results indicate that for the SSCP specimen tested, perpendicular orientation water impacts are more critical than parallel orientations.

#### 4.6. Parametric sweep of slamming orientations

To investigate the effects of slamming orientations on SSCP strain states, a parametric sweep of impact orientation angles,  $\alpha$ , was conducted. The SSCP specimen was tested from 0° (parallel) to 90° (perpendicular) orientation angles in 5° increments, for a total of 19 tests. Strain predictions at each gauge location were recorded (Fig. 15). Pressure distributions based on the 2D asymptotic solution by Zhao and Faltinsen (1993) (Eqs. (4)–(6)) were mapped to the FEA model for a 10° deadrise angle at 2 m/s, producing a 2.5D impact scenario.

$$\text{for } 0 \leq x \leq c(t), P(x) = \frac{\rho V c \frac{dc}{dt}}{\sqrt{c^2 - x^2}} - \frac{\rho V c \frac{dc}{dt}}{\sqrt{2c(c-x)}} + \frac{2\rho(\frac{dc}{dt})^2 \sqrt{|\tau|}}{(1 + \sqrt{|\tau|})^2} \quad (4)$$

$$\text{for } x \geq c(t), P(x) = \frac{2\rho(\frac{dc}{dt})^2 \sqrt{|\tau|}}{(1 + \sqrt{|\tau|})^2} \quad (5)$$

$$\text{where, } x - c = \frac{\delta}{\pi} (-\ln |\tau| - 4\sqrt{|\tau|} - |\tau| + 5), \text{ and } \delta = \frac{2\pi c V^2}{(4 \frac{dc}{dt})^2} \quad (6)$$

where  $x$  is the horizontal distance from the keel,  $V$  is the vertical impact velocity,  $c$  is the horizontal wetted length,  $\tau$  is a solution parameter defined by Zhao and Faltinsen (1993) and  $\delta$  is the water jet thickness.

The use of a 2.5D water impact was necessary to apply a constant pressure peak and distribution for each slamming orientation. The complexity of 3D flows around a square panel for oblique impact orientations meant each test would have a different pressure peak and distribution. This would have complicated the comparisons between different tests. Additionally, a 2.5D pressure distribution is likely more representative of the in-service loads for ocean-racing yachts. Water

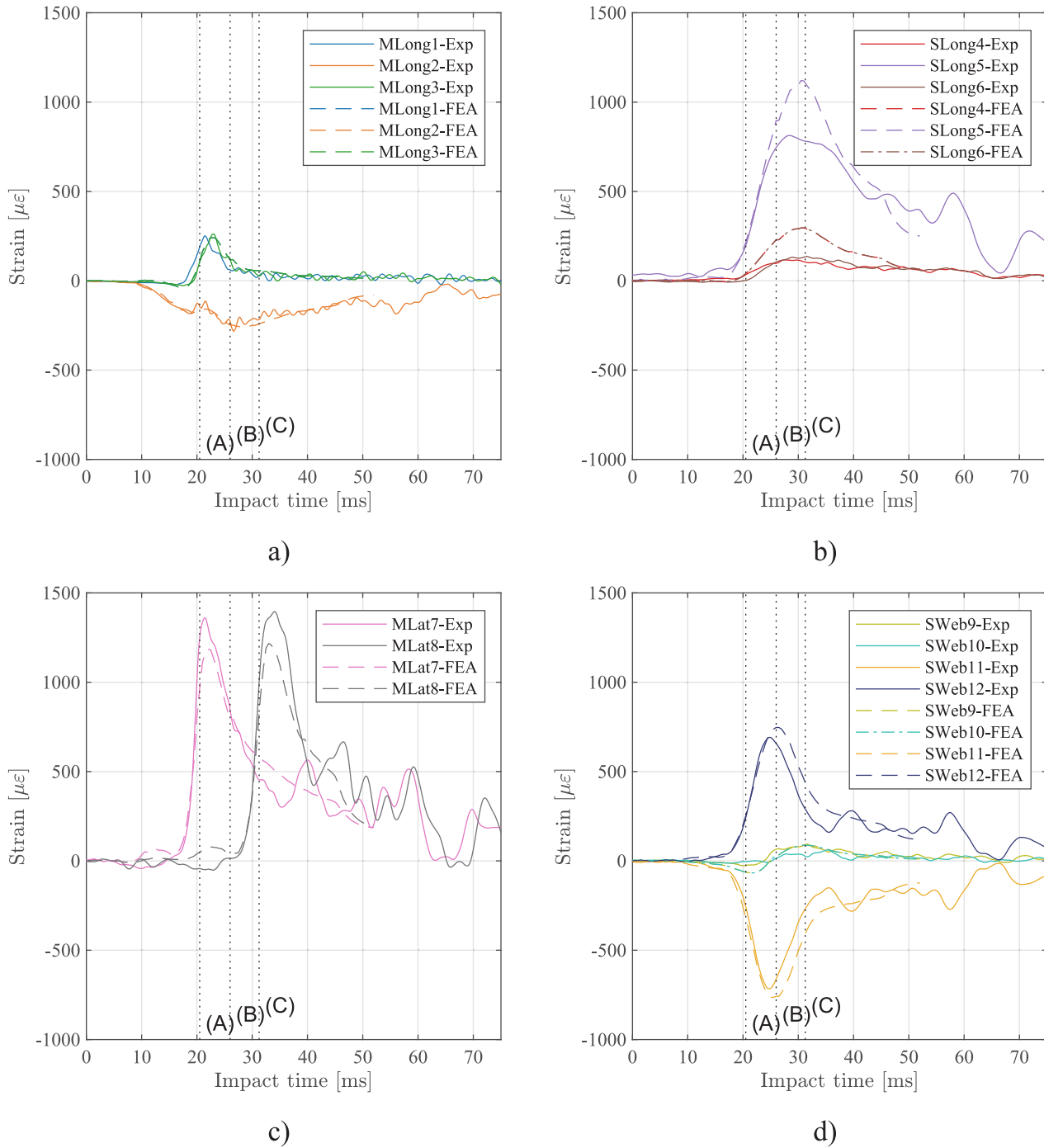


Fig. 20. Experimental and numerical strains from a perpendicular flow impact at  $2 \text{ ms}^{-1}$  (a) Longitudinal monolithic skin strains (b) Longitudinal stringer capping strains, (c) Lateral monolithic skin strains and (d) Stringer web shear strains.

**Table 6**  
Maximum experimental strains in parallel and perpendicular orientations.

	Parallel strains ( $\mu\epsilon$ )	Perpendicular strains ( $\mu\epsilon$ )	% increase
Longitudinal monolithic skin	550	$\pm 250$	-54.5%
Longitudinal stringer capping	690	810	17.4%
Lateral monolithic skin	1100	1390	26.3%
Web shear	430	700	62.8%

impacts of a full hull form are 3D, but from the perspective of a single panel, the flow is 2.5D (Battley and Allen, 2012). Pressure contours at 10, 20, and 30 ms through the chines-dry impact event are shown

in Fig. 24. By comparing Figs. 10 and 24, the difference in pressure distributions between a 2.5D and 3D can clearly be seen. The pressure pulse position and magnitude for a 3D impact lags behind the 2.5D

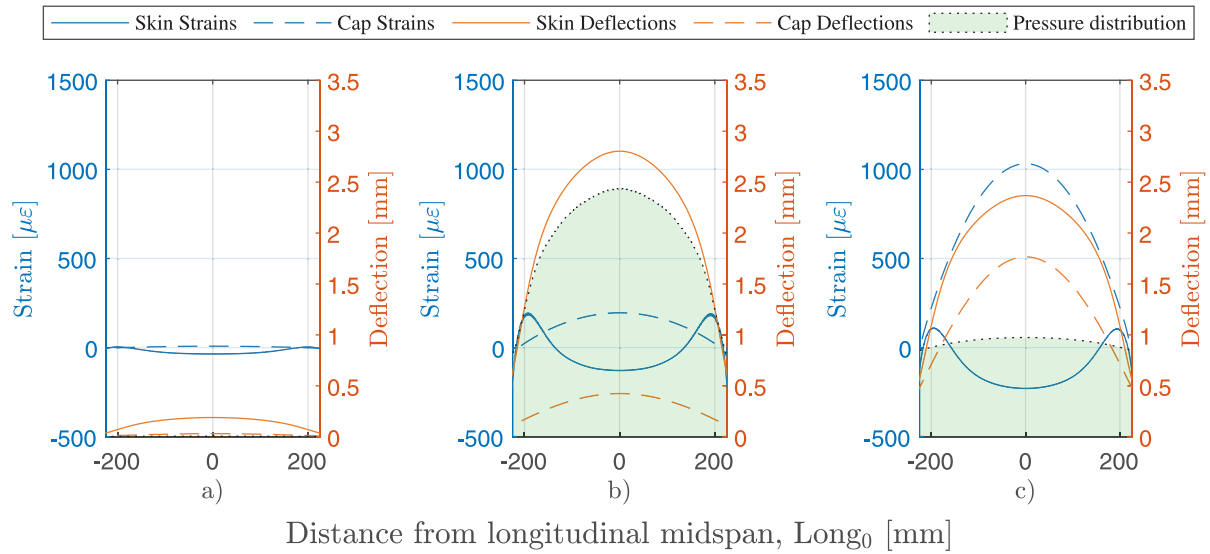


Fig. 21. Longitudinal monolithic skin and stringer strains and deflections for perpendicular orientation impacts with representative pressure distributions at (a) time = 10 ms, (b) time = 20 ms, (c) time = 30 ms.

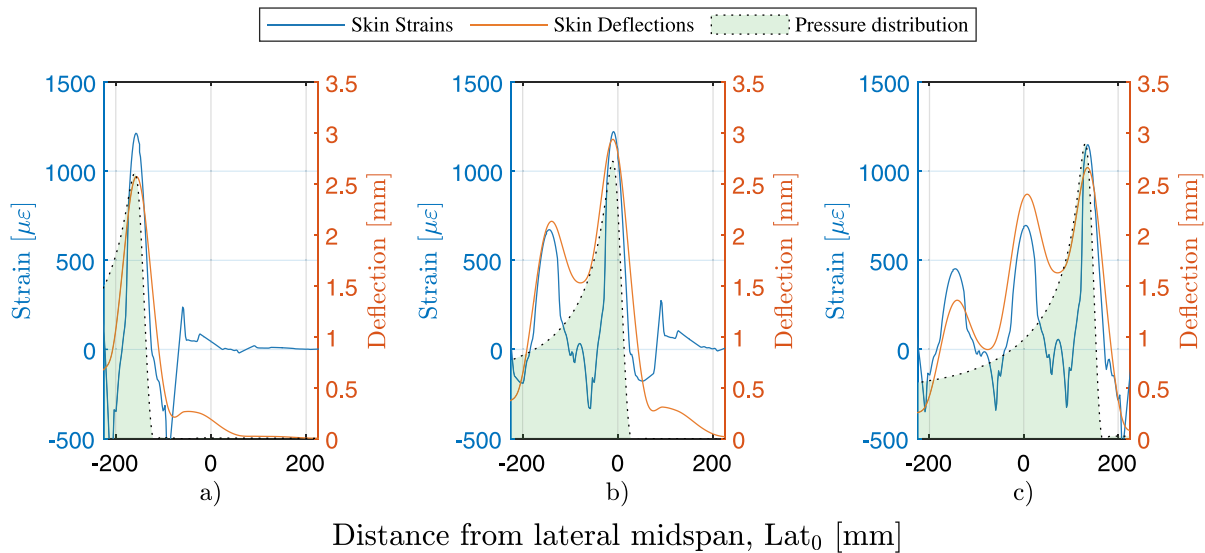


Fig. 22. Lateral monolithic skin strains and deflections for perpendicular orientation impacts with representative pressure distributions at (a) time = 10 ms, (b) time = 20 ms, (c) time = 30 ms.

case, and there are pressure drops along the panel edges compared to the centre. As the body descends into the water in a 3D impact, the displaced water can now evacuate into an additional dimension. This reduces the velocities of the displaced water, thereby reducing the velocity and pressure of the pulse. Reduced structural strains and impact forces are expected for the 3D impact compared to a 2.5D impact. Peak and residual pressures have increased by 255% (58.8 kPa to 150 kPa) and 333% (10.5 kPa to 35.0 kPa) from the 3D to the 2.5D impact case. Maximum impact force has increased by 322% from 6.18 kN to 19.9 kN. Overall, a 2.5D impact involves higher forces and pressures in a faster impact event. A comparison of critical strains (lateral monolithic skin, longitudinal stringer capping and longitudinal stringer web shear) based on 3D and 2.5D impact pressures is presented in Fig. 25. Based on a 2.5D impact pressure, the maximum recorded strains in both parallel and perpendicular orientations occurs in the longitudinal stringer cap, rather than the lateral monolithic skin (as seen for 3D impact pressures). Maximum strains have increased by 67%

from 1028  $\mu\epsilon$  (MLat7) to 1720  $\mu\epsilon$  (SLong5) for parallel orientations, and by 80% from 1218  $\mu\epsilon$  (MLat8) to 2196  $\mu\epsilon$  (SLong5) for perpendicular impacts.

Fig. 26 highlights maximum strains measured at each gauge location with changes of orientation angle. For critical strain measurements, such as lateral skin (MLat7 and MLat8), longitudinal capping (SLong5) and web shear at the supports (SWeb11 and SWeb12), there is an approximately linear relationship between maximum strain and orientation angle. At each critical gauge location, maximum strains in an impact increase as orientation angle increases. This relationship peaks at orientation angles 70–90°, with maximum stringer capping strains occurring at 75° and maximum lateral skin and web shear strains occurring at 80–85°. These maxima occur due to torsional loading of the stringers. At orientation angles 70–90°, the loads from the pressure pulse are concentrated on a single stringer but are not aligned with the stringer axis. This causes bending and torsional loads on the stringer, resulting in higher maximum strains than a perpendicular orientation ( $\alpha = 90^\circ$ ).

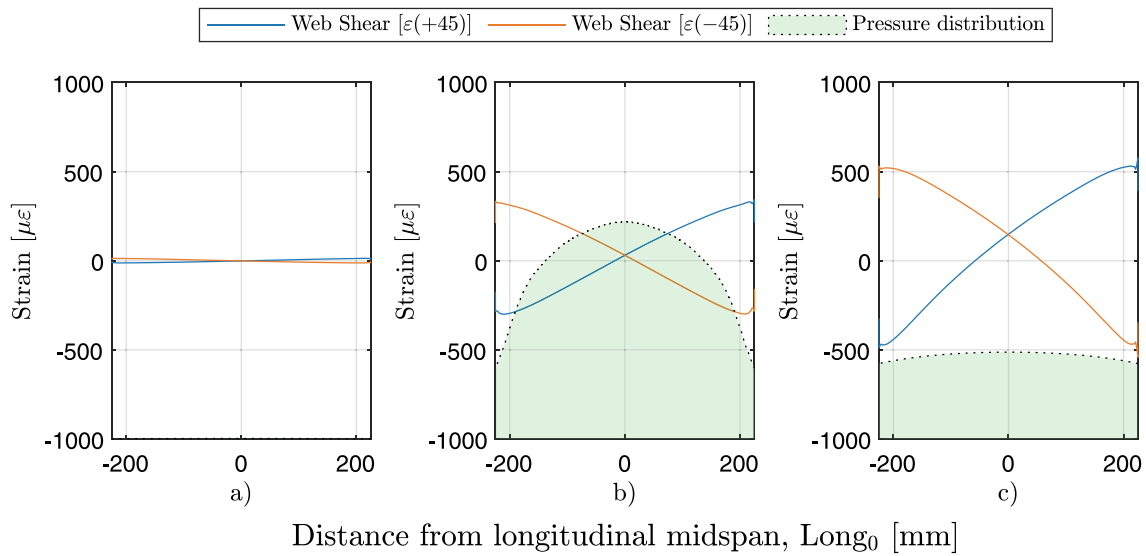


Fig. 23. Longitudinal stringer web shear strains for perpendicular orientation impacts with representative pressure distributions at (a) time = 10 ms, (b) time = 20 ms, (c) time = 30 ms.

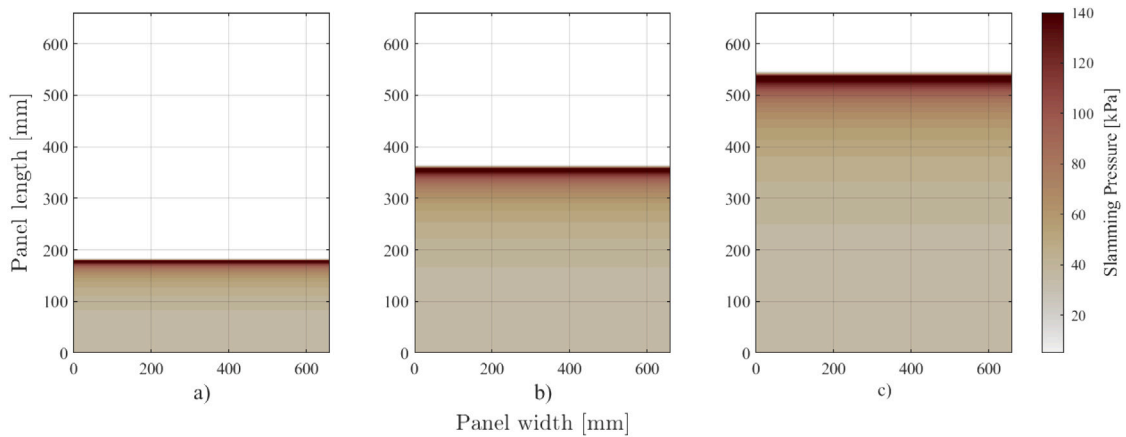


Fig. 24. Pressure distribution for a 2.5D water impact at (a) 10.0 ms (b) 20.0 ms and (c) 30.0 ms.

Maximum longitudinal capping strains (SLong5) at 75° are 2.5% higher than those recorded at 90° orientation angles (2225 μϵ vs. 2170 μϵ) (Fig. 26). Maximum web shear strains (SWeb11) at 80° are 3.0% higher than those recorded at 90° orientation angles (-1414 μϵ vs. 1374 μϵ). Note how the difference between MLat7 and MLat8 (Fig. 26) increases with flow orientation. This occurs as the panel is more loaded once the pressure pulse reaches MLat8 compared to when it reaches MLat7 as the orientation angle increases. Peak strains at MLong1, MLong2 and MLong3 in Fig. 26 are relatively constant for all orientation angles. This implies that maximum longitudinal monolithic skin strains are insensitive to orientation angles. Fig. 27 presents maximum stringer capping and web shear strain profiles along the longitudinal axis for a range of orientation angles. The effects of torsional loading can be seen in Fig. 27b as the shear gradient along the stringer length is not constant.

### 5. Conclusions

This study has conducted an experimental and numerical investigation into the influence of flow-front orientation on the structural response of marine-based SSCPs in constant velocity water impacts. The key findings of this work are given as follows:

- The structural response of SSCPs in water impacts is a superposition of global and local bending mechanisms that are governed by the total impact load and location of the pressure pulse.
- In parallel orientation impacts, the unsupported monolithic skin region between stringers is dominated by the local bending, while stringer capping and shear responses are dominated by overall impact loads.
- In perpendicular orientation impacts, the skin and stringer strain responses are dominated by the presence of the pressure pulse as the entire panel longitudinal span is loaded simultaneously.
- At all angles of impact orientation, the most critical strain responses are the lateral skin, longitudinal stringer capping and longitudinal stringer web shear.
- For the SSCP specimen tested in this study, the most critical structural strains in water impacts are midspan longitudinal capping strains, midspan lateral unsupported monolithic skin strains and web shear strains at the supports. An approximately linear, positive relationship exists between these strain responses and impacting flow orientations. The largest strain responses are observed at high angles of impact orientation (70–90°). The presence of torsional effects in the stringer at 80° < 90° orientation angles can result in higher strains than at 90°.

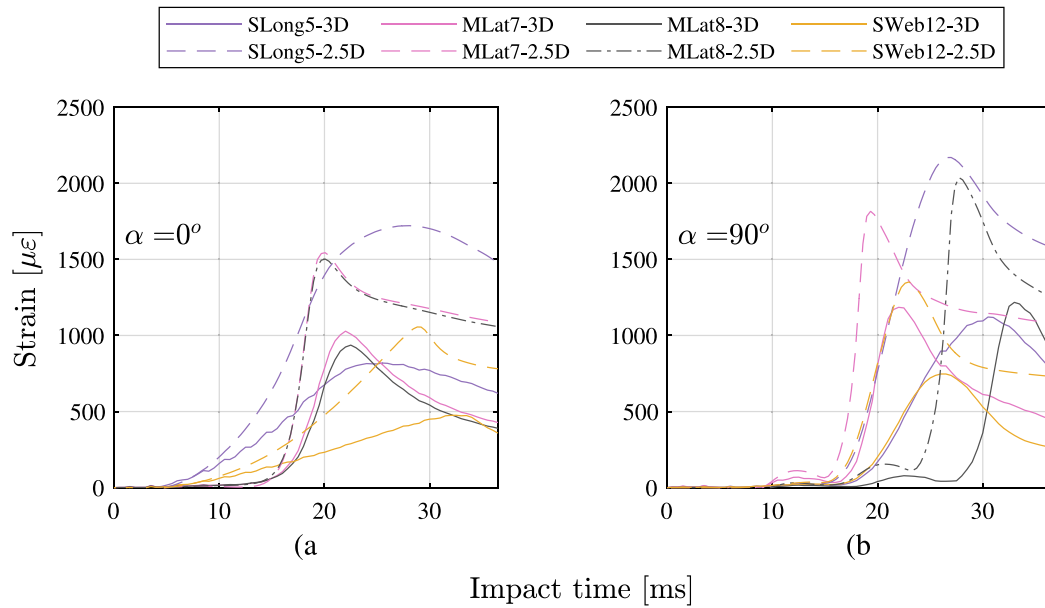


Fig. 25. A comparison of critical strains based on FEA results for 3D and 2.5D impact pressures in (a) Parallel orientation impacts ( $\alpha = 0^\circ$ ) and (b) Perpendicular orientation impacts ( $\alpha = 90^\circ$ ).

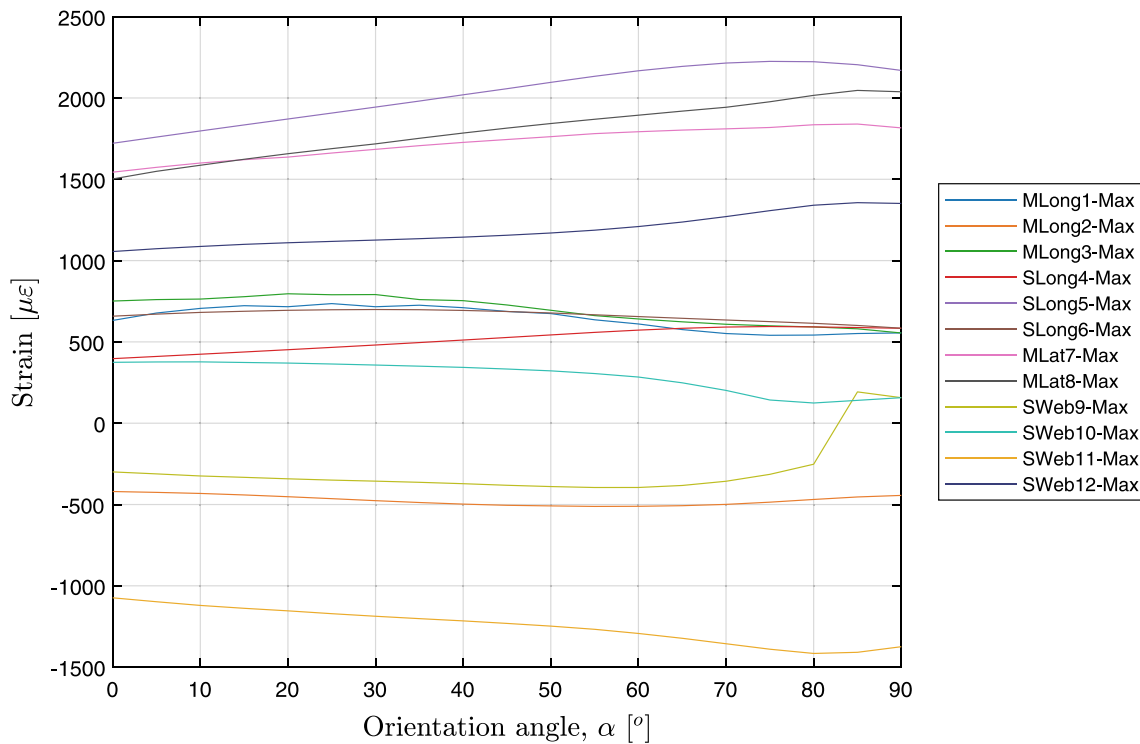


Fig. 26. Maximum absolute strains as a function of flow-front orientation.

The relationships between peak structural strains and flow orientation angles reported in this work are expected to exist for other SSCP configurations and designs. For all configurations, maximum structural strains will occur at, or close to perpendicular orientations as the monolithic skin and stringers are loaded along their entire length by the propagating pressure pulse. Increasing the length of the stringers is expected to increase the difference between parallel and perpendicular orientations as the distance which the pressure pulse can act on is

larger. Increasing the spacing between stringers increases the size of the unsupported monolithic skin region, making it more prone to the effects of pressure pulse induced local bending. Changes to laminates sequences or stringer cross-sectional profiles will modify the structural response, but longitudinal capping, web shear and lateral panel strains are expected to remain the most critical for all configurations despite some reshuffling of relative importance.

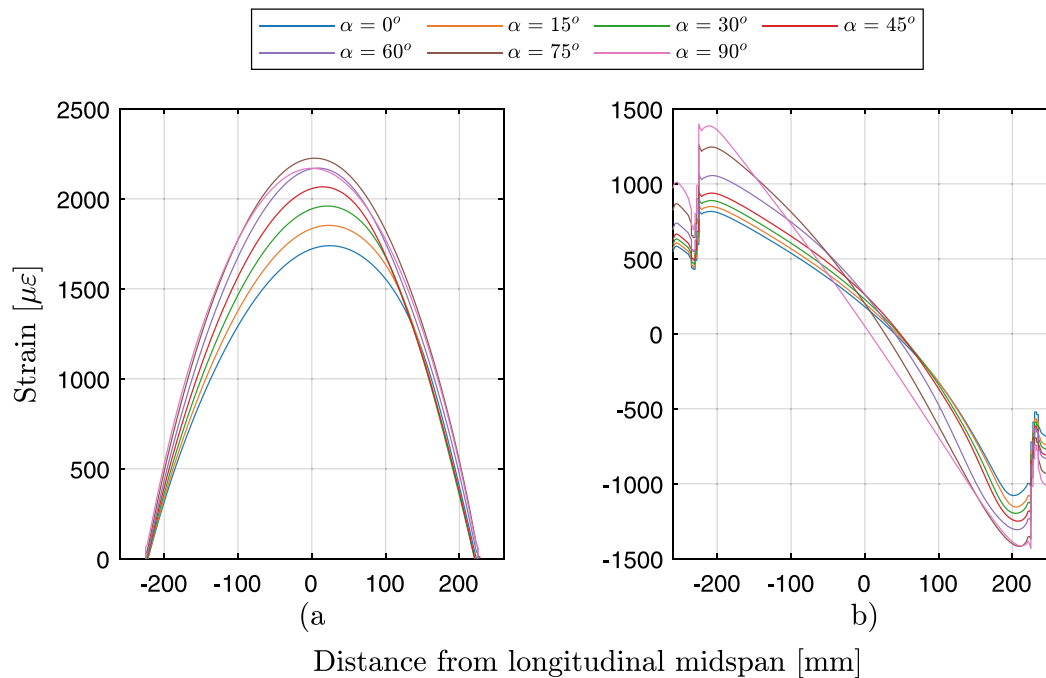


Fig. 27. Maximum strain profiles along the longitudinal SSCP axis for a range of orientation angles for (a) stringer capping strains and (b) stringer web shear strains.

#### CRediT authorship contribution statement

**Connor Pearson:** Writing – review & editing, Writing – original draft, Visualization, Validation, Methodology, Investigation, Formal analysis, Data curation, Conceptualization. **Marius de Mourgues:** Writing – original draft, Writing – review & editing, Methodology, Investigation, Formal analysis, Data curation, Conceptualization. **Mark Battley:** Conceptualization, Resources, Supervision, Writing – review & editing. **Veronique Michaud:** Conceptualization, Supervision, Writing – review & editing. **John Little:** Conceptualization, Resources. **Guillaume Verdier:** Conceptualization, Resources. **Tom Allen:** Conceptualization, Project administration, Resources, Supervision, Writing – review & editing.

#### Declaration of competing interest

The authors declare that they have no known competing financial interests or personal relationships that could have appeared to influence the work reported in this paper.

#### Data availability

Data will be made available on request.

#### Use of AI statement

No generative AI was used in the writing of this document.

#### Acknowledgements and funding sources

The authors would like to acknowledge Xueliang Wen from the University of Stavanger for his help and guidance with setting up the GMM CFD models.

This work is funded by the University of Auckland Doctoral Scholarship, which covers all associated costs associated with this research. This research did not receive any specific grant from funding agencies in the public, commercial, or not-for-profit sectors.

#### Appendix A. Supplementary data

Supplementary material related to this article can be found online at <https://doi.org/10.1016/j.oceaneng.2024.117797>.

#### References

- Abrate, S., 2011. Hull slamming. *Appl. Mech. Rev.* 64 (6), 1–35.
- Ahmadi, H., Rahimi, G., 2019. Analytical and experimental investigation of transverse loading on grid stiffened composite panels. *Composites B* 159 (September 2018), 184–198. <http://dx.doi.org/10.1016/j.compositesb.2018.09.040>.
- Allen, T., 2013. *Mechanics of Flexible Composite Hull Panels Subjected to Water Impacts* (Ph.D. thesis). University of Auckland.
- Allen, T., Battley, M., 2015. Quantification of hydroelasticity in water impacts of flexible composite hull panels. *Ocean Eng.* 100, 117–125. <http://dx.doi.org/10.1016/j.oceaneng.2015.04.012>.
- Allen, R.G., Jones, R.R., Taylor, D.W., 1978. A simplified method for determining structural design-limit pressures on high performance marine vehicles. In: *AIAA/SNAME Advanced Marine Vehicles Conference*. San Diego, California, pp. 1–11.
- Battley, M., Allen, T., 2012. Servo-hydraulic system for controlled velocity water impact of marine sandwich panels. *Exp. Mech.* 52 (1), 95–106. <http://dx.doi.org/10.1007/s11340-011-9543-7>.
- Battley, M., Allen, T., Pehrson, P., Stenius, I., Rosén, A., 2009. Effects of panel stiffness on slamming responses of composite hull panels. In: *International Conference on Composite Materials*. pp. 1–11.
- Battley, M., Stenius, I., Breder, J., Edinger, S., 2005. Dynamic characterisation of marine sandwich structures. In: *Sandwich Structures 7: Advancing with Sandwich Structures and Materials*. Springer-Verlag, pp. 537–546. [http://dx.doi.org/10.1007/1-4020-3848-8\\_54](http://dx.doi.org/10.1007/1-4020-3848-8_54).
- Berezniński, A., 2001. Slamming: the role of hydroelasticity. *Int. Shipbuild. Progress* 48, 333–351.
- Bertolini, J., Castanié, B., Barrau, J.J., Navarro, J.P., 2008. An experimental and numerical study on omega stringer debonding. *Compos. Struct.* 86 (1–3), 233–242. <http://dx.doi.org/10.1016/j.compstruct.2008.03.013>.
- Blázquez, A., Reinoso, J., París, F., Cañas, J., 2012. Postbuckling behavior of a pressurized stiffened composite panel – part II: Numerical analysis. Effect of the geometrical imperfections. *Compos. Struct.* 94 (5), 1544–1554. <http://dx.doi.org/10.1016/j.compstruct.2011.12.013>, URL <https://www.sciencedirect.com/science/article/pii/S0263822311004818>.
- Charca, S., Shafiq, B., 2010. Damage assessment due to single slamming of foam core sandwich composites. *J. Sandw. Struct. Mater.* 12 (1), 97–112. <http://dx.doi.org/10.1177/1099636209105402>.

- Charca, S., Shafiq, B., 2011. Damage assessment due to repeated slamming of foam core sandwich composites. *J. Sandw. Struct. Mater.* 13 (1), 97–109. <http://dx.doi.org/10.1177/1099636209344131>.
- Charca, S., Shafiq, B., Just, F., 2009. Repeated slamming of sandwich composite panels on water. *J. Sandw. Struct. Mater.* 11 (5), 409–424. <http://dx.doi.org/10.1177/1099636209103169>.
- Chen, Z., Jiao, J., Wang, S., Guedes Soares, C., 2023. CFD-FEM simulation of water entry of a wedged grillage structure into Stokes waves. *Ocean Eng.* 275, 114159. <http://dx.doi.org/10.1016/j.oceaneng.2023.114159>, URL <https://www.sciencedirect.com/science/article/pii/S0029801823005437>.
- Chuang, S.-L., 1966a. Experiments on flat-bottom slamming. *J. Ship Res.* 10 (01), 10–17. <http://dx.doi.org/10.5957/jsr.1966.10.1.10>.
- Chuang, S.-L., 1966b. Slamming of rigid wedge-shaped bodies with various deadrise angles. Technical Report October, Structural Mechanics Laboratory Research and Development.
- DNV-GL, 2015. Part 3 - structures, equipment, chapter 1 - design principles, design loads.
- Duan, L., Zhu, L., Chen, M., Pedersen, P.T., 2020. Experimental study on the propagation characteristics of the slamming pressures. *Ocean Eng.* 217, 107868. <http://dx.doi.org/10.1016/j.oceaneng.2020.107868>, URL <https://www.sciencedirect.com/science/article/pii/S0029801820308362>.
- Faltinsen, O.M., Landrini, M., Greco, M., 2004. Slamming in marine applications. *J. Eng. Math.* 48 (3–4), 187–217. <http://dx.doi.org/10.1023/b:engi.0000018188.68304.ae>.
- Fondelli, T., Andreini, A., Facchini, B., 2015. Numerical simulation of dam-break problem using an adaptive meshing approach. In: *Energy Procedia*. Vol. 82, Elsevier Ltd, pp. 309–315. <http://dx.doi.org/10.1016/j.egypro.2015.12.038>.
- Hassoon, O.H., Tarfaoui, M., El Malki Alaoui, A., El Moumen, A., 2017a. Experimental and numerical investigation on the dynamic response of sandwich composite panels under hydrodynamic slamming loads. *Compos. Struct.* 178, 297–307. <http://dx.doi.org/10.1016/j.compstruct.2017.07.014>.
- Hassoon, O.H., Tarfaoui, M., El Malki Alaoui, A., El Moumen, A., 2018. Mechanical behavior of composite structures subjected to constant slamming impact velocity: An experimental and numerical investigation. *Int. J. Mech. Sci.* 144, 618–627. <http://dx.doi.org/10.1016/j.iijmecsci.2018.05.035>.
- Hassoon, O.H., Tarfaoui, M., El Moumen, A., Benyahia, H., Nachtane, M., 2017b. Numerical evaluation of dynamic response for flexible composite structures under slamming impact for naval applications. *Appl. Compos. Mater.* 25 (3), 689–706. <http://dx.doi.org/10.1007/s10443-017-9646-0>.
- Hassoon, O.H., Tarfaoui, M., El Moumen, A., Qureshi, Y., Benyahia, H., Nachtane, M., 2019. Mechanical performance evaluation of sandwich panels exposed to slamming impacts: Comparison between experimental and SPH results. *Compos. Struct.* 220, 776–783. <http://dx.doi.org/10.1016/j.compstruct.2019.04.051>.
- Hirt, C.W., Nichols, B.D., 1981. Volume of fluid (VOF) method for the dynamics of free boundaries. *J. Comput. Phys.* 39 (1), 201–225. [http://dx.doi.org/10.1016/0021-9991\(81\)90145-5](http://dx.doi.org/10.1016/0021-9991(81)90145-5).
- Hosseinzadeh, S., Tabri, K., Hirdaris, S., Sakh, T., 2023a. Slamming loads and responses on a non-prismatic stiffened aluminium wedge: Part I. Experimental study. *Ocean Eng.* 279, 114510. <http://dx.doi.org/10.1016/j.oceaneng.2023.114510>, URL <https://www.sciencedirect.com/science/article/pii/S0029801823008946>.
- Hosseinzadeh, S., Tabri, K., Topa, A., Hirdaris, S., 2023b. Slamming loads and responses on a non-prismatic stiffened aluminium wedge: Part II. Numerical simulations. *Ocean Eng.* 279, 114309. <http://dx.doi.org/10.1016/j.oceaneng.2023.114309>, URL <https://www.sciencedirect.com/science/article/pii/S0029801823006935>.
- International monohull open class association (IMOCA), 2021. IMOCA Class Rule 2021. ISO, 2019. Part 5: Design pressures for monohulls, design stresses, scantlings determination. In: *ISO 12215-5 Small Craft - Hull Construction and Scantlings*.
- Jin, B.C., Li, X., Mier, R., Pun, A., Joshi, S., Nutt, S., 2015. Parametric modeling, higher order FEA and experimental investigation of hat-stiffened composite panels. *Compos. Struct.* 128, 207–220. <http://dx.doi.org/10.1016/j.compstruct.2015.03.068>.
- Li, K.-y., 2018. Prediction Of Structural Responses Of Flexible Polymer Hull Undergoing Water Impacts Using Coupled Eulerian- Lagrangian Analysis (Ph.D. thesis). University of Auckland.
- Li, B., Gong, Y., Gao, Y., Hou, M., Li, L., 2022. Failure analysis of hat-stringer-stiffened aircraft composite panels under four-point bending loading. *Materials* 15 (7), 2430. <http://dx.doi.org/10.3390/MA15072430>, [https://www.mdpi.com/1996-1944/15/7/2430](https://www.mdpi.com/1996-1944/15/7/2430/html).
- Mo, Y., Ge, D., He, B., 2016. Experiment and optimization of the hat-stringer-stiffened composite panels under axial compression. *Composites B* 84, 285–293. <http://dx.doi.org/10.1016/j.compositesb.2015.08.039>.
- Nair, V.V., Bhattacharyya, S.K., 2018a. Water entry and exit of axisymmetric bodies by CFD approach. *J. Ocean Eng. Sci.* 3 (2), 156–174. <http://dx.doi.org/10.1016/j.joes.2018.05.002>.
- Nair, V.V., Bhattacharyya, S.K., 2018b. Water impact of three dimensional wedges using CFD. *Ocean Syst. Eng.* 8 (2), 223–246. <http://dx.doi.org/10.12989/ose.2018.8.2.223>.
- Pearson, C.A., Allen, T.D., Battley, M.A., 2022. Numerical water impacts of 2D hull forms using dynamic overset meshing. *J. Sail. Technol.* 7 (01), 228–254. <http://dx.doi.org/10.5957/jst/2022.7.11.228>, [arXiv:https://onpetro.org/JST/article-pdf/7/01/228/3057508/sname-jst-2022-11.pdf](https://onpetro.org/JST/article-pdf/7/01/228/3057508/sname-jst-2022-11.pdf).
- Qu, Q., Hu, M., Guo, H., Liu, P., Agarwal, R., 2015. Study of ditching characteristics of transport aircraft by global moving mesh method. *J. Aircr.* 52 (5), 1550–1558.
- Reinoso, J., Blázquez, A., París, F., Cañas, J., Meléndez, J., 2012. Postbuckling behaviour of a pressurized stiffened composite panel – part I: Experimental study. *Compos. Struct.* 94 (5), 1533–1543. <http://dx.doi.org/10.1016/j.compstruct.2011.12.014>, URL <https://www.sciencedirect.com/science/article/pii/S026382231100482X>.
- Stenius, I., Rosén, A., Battley, M., Allen, T., 2013. Experimental hydroelastic characterization of slamming loaded marine panels. *Ocean Eng.* 74, 1–15. <http://dx.doi.org/10.1016/j.oceaneng.2013.09.007>.
- Stenius, I., Rosén, A., Kuttenukeuler, J., 2007. Explicit FE-modelling of hydroelasticity in panel-water impacts. *Int. Shipbuild. Prog.* 54 (2–3), 111–127.
- Stenius, I., Rosén, A., Kuttenukeuler, J., 2011. Hydroelastic interaction in panel-water impacts of high-speed craft. *Ocean Eng.* 38 (2–3), 371–381. <http://dx.doi.org/10.1016/j.oceaneng.2010.11.010>.
- Swidan, A., Thomas, G., Penesis, I., Ranmuthugala, D., Amin, W., Allen, T., Battley, M., 2017. Wetdeck slamming loads on a developed catamaran hullform—experimental investigation. *Ships Offshore Struct.* 12 (5), 653–661. <http://dx.doi.org/10.1080/17445302.2016.1194555>, URL <https://www.tandfonline.com/doi/full/10.1080/17445302.2016.1194555>.
- Swidan, A., Thomas, G., Ranmuthugala, D., Amin, W., Penesis, I., Allen, T., Battley, M., 2016. Experimental drop test investigation into wetdeck slamming loads on a generic catamaran hullform. *Ocean Eng.* 117, 143–153. <http://dx.doi.org/10.1016/j.oceaneng.2016.03.059>.
- Tveitnes, T., Fairlie-Clarke, A.C., Varyani, K., 2008. An experimental investigation into the constant velocity water entry of wedge-shaped sections. *Ocean Eng.* 35 (14–15), 1463–1478. <http://dx.doi.org/10.1016/j.oceaneng.2008.06.012>.
- Vescovini, R., Dávila, C.G., Bisagni, C., 2013. Failure analysis of composite multi-stringer panels using simplified models. *Composites B* 45 (1), 939–951. <http://dx.doi.org/10.1016/j.compositesb.2012.07.030>.
- von Karman, T., 1929. *The Impact on Seaplane Floats During Landing*. Technical Report, USA: National Advisory Committee for Aeronautics.
- Wagner, H., 1931. *Landing of seaplanes*. Technical Report, USA: National Advisory Committee for Aeronautics, p. 32.
- Weber, J.B., 2017. *The Role of Curvature and Structural Compliance on Water Impact Loading of Composite Structures* (Ph.D. thesis). University of Auckland, p. 192.
- Wen, X., Ong, M.C., Yin, G., 2023. On the three-dimensional effects of the water entry of wedges. *Appl. Ocean Res.* 138, 103649. <http://dx.doi.org/10.1016/j.apor.2023.103649>, URL <https://www.sciencedirect.com/science/article/pii/S0141118723001906>.
- Wen, X., P., L., Del Buono, A., Qu, Q., Iafrazi, A., 2022. Formulations of hydrodynamic force in the transition stage of the water entry of linear wedges with constant and varying speeds. *J. Fluids Struct.* 115, 103759. <http://dx.doi.org/10.1016/j.jfluidstruct.2022.103759>, URL <https://www.sciencedirect.com/science/article/pii/S0889974622001517>.
- Zhao, R., Faltinsen, O.M., 1993. Water entry of two-dimensional bodies. *J. Fluid Mech.* 246 (4), 593–612. <http://dx.doi.org/10.1017/S002211209300028X>.
- Zhu, S., Yan, J., Chen, Z., Tong, M., Wang, Y., 2015. Effect of the stiffener stiffness on the buckling and post-buckling behavior of stiffened composite panels - Experimental investigation. *Compos. Struct.* 120, 334–345. <http://dx.doi.org/10.1016/j.compstruct.2014.10.021>.
- Zimmermann, R., Klein, H., Kling, A., 2006. Buckling and postbuckling of stringer stiffened fibre composite curved panels - Tests and computations. *Compos. Struct.* 73 (2), 150–161. <http://dx.doi.org/10.1016/j.compstruct.2005.11.050>.